Project Title: Effect of H_2S and CO_2 in HPHT Wells on Tubulars and Cement

Report Type: Monthly Report

Report #: 09

Reporting Period: May 22nd, 2012 to June 21st, 2012

Authors:

Ramadan Ahmed, Principal Investigator

Subhash Shah, Co-Principal Investigator

Samuel Osisanya, Co-Principal Investigator

Shokrollah Hassani, Postdoctoral Research Associate

Majed Enfis, Research Assistant

Rida Elgaddafi, Research Assistant

Himanshu Maheshwari, Research Assistant

Adarsh Naidu, Research Assistant

Prepared under BSEE Project # E12PC00035

by

THE UNIVERSITY OF OKLAHOMA

July 18, 2012

1. Summary of Accomplishments

This monthly report presents the progress made during the project period May 22, 2012 – June 21, 2012. The development of experimental setups for testing cement degradation has been completed. Testing of the aging cell and compressive strength measuring setup has been completed. Cored specimens have been prepared to carry out the aging experiments that will begin in the coming days. Literature review, and theoretical and modeling studies on tubular degradation is in progress. Moreover, in order to predict the amount of calcium present in the cement (initial calcium concentration) after curing, cement hydration models were investigated. The initial calcium concentration is necessary to predict the degradation depth, mechanical properties, and permeability of the cement. A report summarizing the results of these studies is presented in Appendix A and B.

Our effort to develop cement specimen preparation procedure was continued. During this reporting period, cement specimens were prepared using fresh water and the effects of sample preparation techniques (i.e. casting and coring) on porosity and permeability of cement specimens were examined. The sample preparation techniques have little effect on porosity and permeability of the specimens. Cored specimens were prepared using more advanced coring machine that has minimal bit vibration and irregularities. Using the new coring machine, uniform samples were prepared. The cored specimens had better quality and geometric uniformity than the casted ones. Beside this, microscopic examination of casted specimens showed the presence of micro cracks.

Porosity predictions were made for the specimens based on free water in cement system after curing using the cement hydration model. Porosity measurements and predictions showed a good agreement. Two different porosity measurement techniques were used for dry and wet specimens. Experimental porosity measurement results were the same for the dry and wet specimens.

Scanning Electron Microscopy (SEM), X-Ray Fluorescence (XRF), and Fourier Transform Infrared Spectroscopy (FTIR) were used to analyze the cement specimen. SEM was used to study different phases in cement including CH, CSH, and unhydrated cement. XRF were used to study different elements and phases in the cement. FTIR measurements taken before and after cement hydration do not show significant differences. We are exploring the possibility of using X-ray Diffraction (XRD) technique to analyze the cement specimens.

Investigation on tubular corrosion is one of the key components of this project. A number of CO_2 and H_2S corrosion models have been reviewed during the past month. Different

empirical, semi-empirical, and mechanistic models are available for CO_2 and H_2S corrosion prediction. Most of the models available in the literature are limited to low-temperature low-pressure conditions. Research is in progress to develop a new mechanistic model for CO_2 and H_2S corrosion rate prediction under high-temperature and high-pressure conditions.

Our plan for the coming weeks is to perform aging experiments. We will continue our theoretical and modeling studies on tubular corrosion as well.

2. Overall Project Progress

2.1 Theoretical Studies (Task 1)

Initial porosity of the cement is an important factor in predicting the leaching rate of the cement and consequently mechanical properties and permeability of the cement. The initial porosity of cement is a function of water-to-cement ratio and degree of hydration. In order to predict the initial porosity of cured specimens, cement hydration model developed by Lin and Meyer (2009) was applied for Classes H and G cements at different temperatures. Predicted porosity measurements show a good agreement with measurements. The degree of hydration versus time plot for different temperatures can be used to determine the appropriate curing time needed to get maximum hydration. Furthermore, the model was used to predict the maximum calcium concentration in classes H and G cements.

Theoretical and modeling studies on corrosion of tubulars were continued. Most commonly used CO_2/H_2S corrosion models were reviewed. There are numerous CO_2 and H_2S corrosion models available in the literature to predict corrosion rate and protective film thickness and properties. However, most of these models are developed for low-temperature and low-pressure applications. The validity of these models at high temperature and pressure conditions has not been verified. Improvements have been proposed to one of the available CO_2 corrosion models (Dayalan et al., 1995). Proposed modifications change some of the basic hypotheses of the model including temperature and pressure limitations. In the coming months, a model will be developed for H_2S corrosion. The Synergistic effect of CO_2 corrosion and H_2S corrosion is also an important area of consideration for combining the two models. Details of theoretical and modeling studies on tubular CO_2 and H_2S corrosion are presented in Appendix B.

2.2 Experimental Studies on Degradation of Cement (Task 2)

The objective of this task is to test the performance of conventional cement under different test conditions. Cement specimen setup and test condition for first set of aging experiment are shown in Fig. 1. Two different classes of cement G and H will be aged under high-pressure

high-temperature conditions (9000 psi and 350°F). Silica is added to the cement to improve the high temperature resistance. Effect of fly ash will be studied for the first set of aging experiment. Fly ash as a cement additive reduces the cost of cement, reduces the slurry density, increases the strength of cement, increases the thickening time, and also reacts with calcium hydroxide and form calcium silicates. Fly ash class F is used in this research because it has lower sulfate content. Amount of fly ash added to the cement is 100% by weight. Two aged cement samples will be used for porosity and permeability testing; they can also be use for FTIR, SEM, and cross sectioning and studying the degradation depth. Three samples will be used for compressive strength testing. First batch of the samples will be removed after 15 days and the second batch will be removed after 30 days. Sample coding is based on the batch number, shelf number, and order number as shown in Fig. 1.

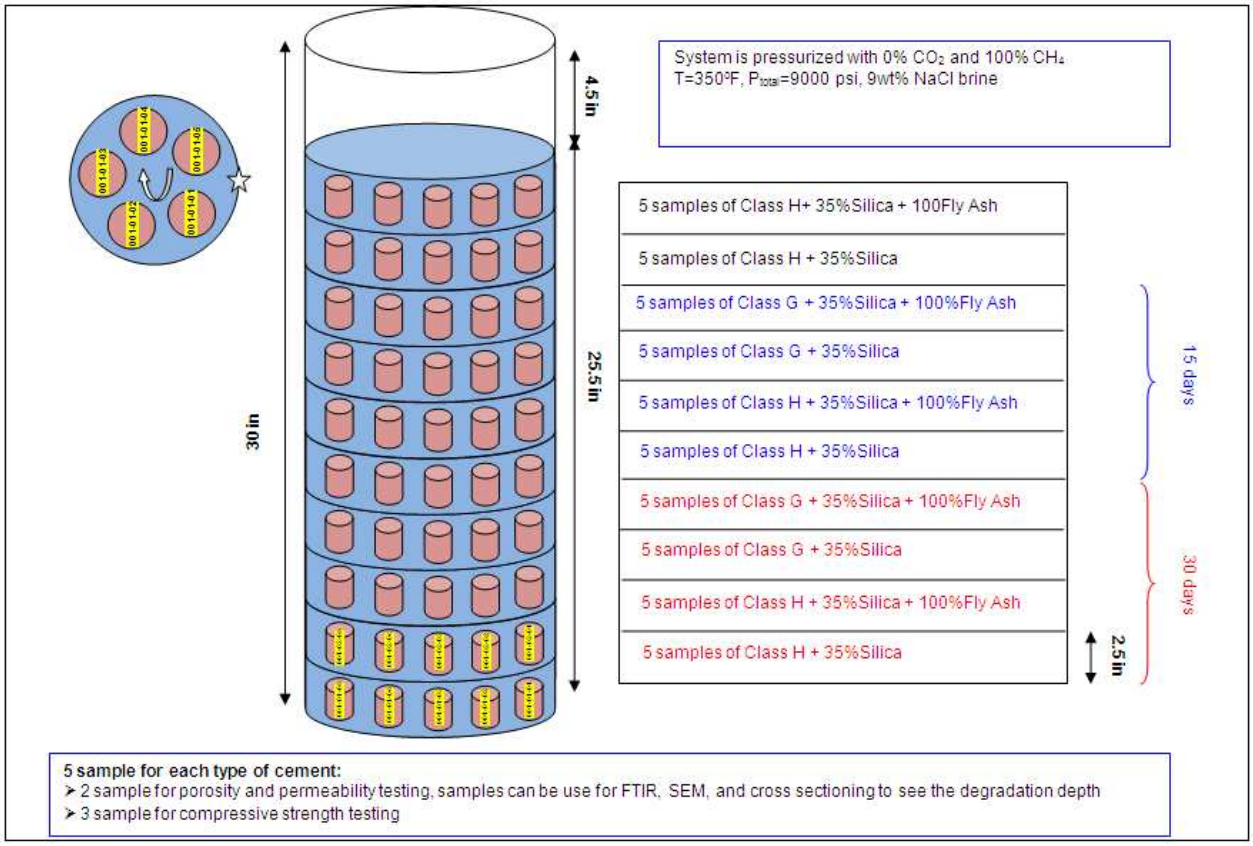

Fig. 1 Cement specimen setup and test condition for first set of aging experiment

The development of an established specimen preparation procedure was continued. Cement slurries with water to cement ratio of 38% were prepared by adding 1.9 lbm of neat Class H cement to 0.72 lbm of tap water (fresh water). The slurry was mixed for 35 seconds

using a standard laboratory agitator. However, API procedure requires using special high speed mixers (4,000 and 12,000 rpm preset speeds) to prepare cement slurries. Thus, a new cement mixer has been purchased to be used during slurry preparation. After preparing the cement slurry, the paste was poured into five identical stainless steel molds (1” Diameter x 2” Length) which were sprayed with silicon release. The paste was also poured in a bigger beaker for preparing the core specimens. Poured paste was left for 24 hours to harden in the moulds and develop the initial strength under ambient conditions. Then, the specimens (cores) were cured in tap water for 5 days at temperature of 200ºF using a large-sized laboratory oven. After curing, the cores were recovered from the moulds and dried to a constant weight. Then, their porosity and permeability were measured. Specimen dimensions, weight, and measured porosity and permeability are shown in Table 1. Results presented in Figs. 2 and 3 show that the effect of sample preparation techniques (i.e. casting or coring) on porosity and permeability of the cement is very minimal. However, coring was selected as the best method for sample preparation because cored specimens were more uniform than the cast ones. In addition, the casted specimens had micro cracks as shown in SEM images. The micro cracks could be as a result of high plunger force needed for taking out the sample out of mold.

Table 1 Porosity-permeability data for different neat cement specimens/cores

	Core dimensions				Porosity				Permeability		Remarks	
Core #	Diameter	Length	Weight (g)		V_b	V_g	V_p	Porosity	K_{air}	K_{klink}		
	mm	mm	Wet	Dry	c.c	c.c	c.c	%	md	md		
20	24.90	27.85		23.96	13.56	9.41	4.15	30.60	0.261	0.180	Cured under 200°F	Mixing Time is 35 seconds
21	24.98	28.83		25.75	14.13	10.34	3.79	26.82	0.201	0.135	Cured under ambient temp.	
22	25.31	29.73		26.91	14.96	10.94	4.02	26.87	0.153	0.098		
23	25.09	31.49		27.02	15.57	10.64	4.93	31.7	0.203	0.136	Cured under 200°F	Mixing Time is 35 seconds
24	25.08	30.92		26.34	15.28	10.51	4.77	31.2	0.239	0.162		
25	25.38	28.88		25.18	14.61	9.85	4.76	32.58	0.180	0.118		
26	24.73	30.42		25.71	14.61	10.1	4.51	30.87	0.219	0.147		
27	24.82	31.51		26.52	15.25	10.38	4.87	31.93	0.135	0.083		
28	24.76	30.30	30.71	26.52	14.59	10.47	4.12	28.24	0.106	0.064	Cured with 3% brine under 200°F, Cement slurry prepared in 3% brine, 2:30 min.	
29	25.15	30.25	30.33	25.57	15.03	10.05	4.98	33.13	0.313	0.220		
30	25.40	30.76	30.98	26.10	15.59	10.52	5.07	32.52	0.208	0.139		
31	25.40	26.46	26.77	22.35	13.41	8.9	4.51	33.63	0.253	0.174		
32	24.65	30.92	29.27	27.99	14.76	11.19	3.57	24.19	0.054	0.03	Slurry in fresh water, cured in 9% brine at 200°F, 2:30 min. (**CASTING**)	
33	25.01	30.14	28.11	26.54	14.81	10.47	4.34	29.30	0.299	0.211		
34	24.68	28.60	26.49	24.96	13.68	9.62	4.06	29.68	0.388	0.282		
35	24.75	28.30	26.11	24.72	13.62	9.68	3.94	28.93	-	-		
36	24.88	28.53	26.34	24.84	13.87	9.99	3.88	27.97	0.287	0.202		
37	25.23	27.03	26.28	23.73	13.51	9.62	3.89	28.79	0.273	0.188	Slurry in fresh water, cured in 9% brine at ambient conditions, 2:30 min. (**CORING**)	
38	25.23	28.29	25.81	24.31	14.14	9.82	4.32	30.55	0.336	0.238		
39	25.26	27.73	26.24	24.01	13.9	9.67	4.23	30.43	0.322	0.227		
40	25.24	29.46	26.99	25.13	14.74	10.12	4.62	31.34	0.372	0.266		
41	25.26	26.83	25.58	23.13	13.45	9.32	4.13	30.71	0.309	0.217		
42	25.25	29.67	27.43	25.73	14.86	10.32	4.54	30.55	0.318	0.223		
43	25.27	30.45	28.53	26.45	15.27	10.61	4.66	30.52	0.292	0.202		
44	25.23	25.95	24.61	22.41	12.97	8.99	3.98	30.69	0.356	0.255		
45	25.24	62.39	57.76	54.18	31.22	21.5	9.72	31.13	0.412	0.287		

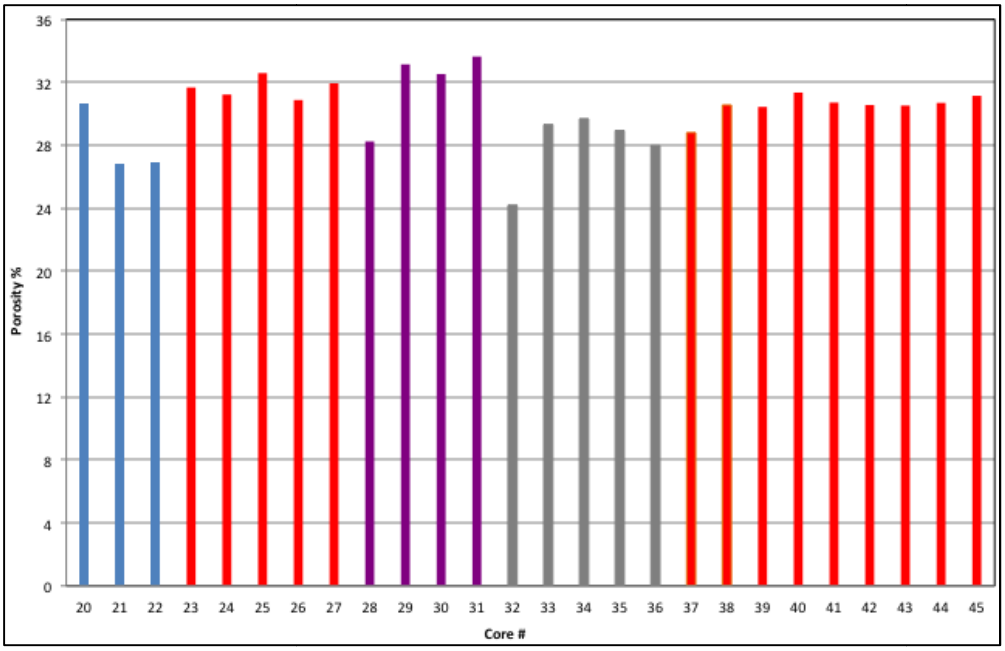

Fig. 2 Porosity measurements

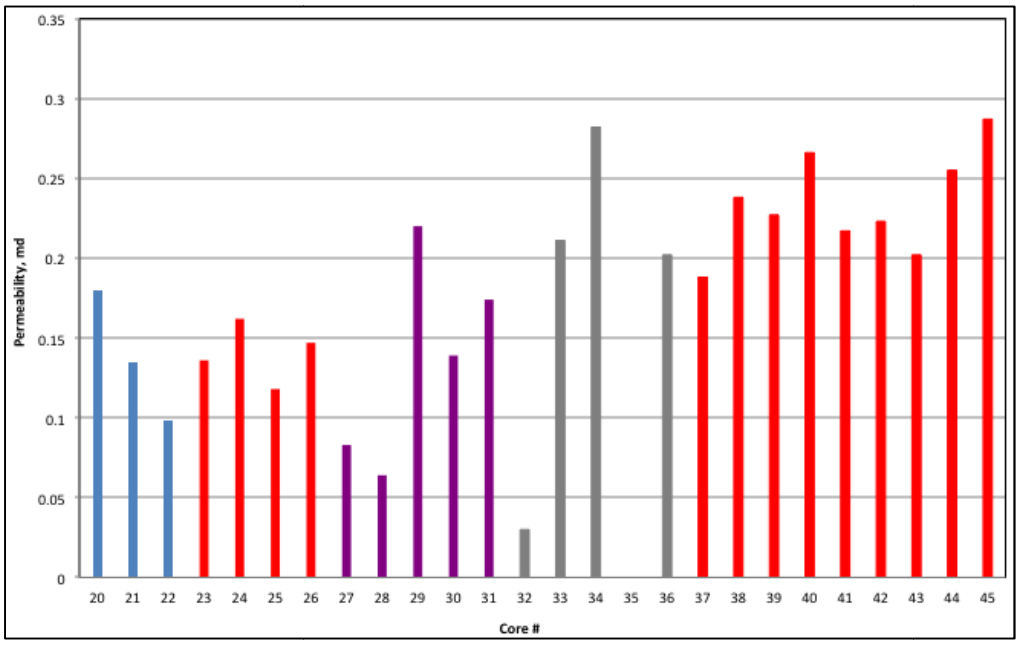

Fig. 3 Permeability measurements

Nuclear magnetic resonance (NMR) and gas porosimeters were used to measure the porosity of wet and dry samples, respectively. Results are shown in Table 2 and Fig. 4. NMR makes use of the Gibbs-Thomson effect, which is based on the assumption that small crystals of a liquid in the pores melt at a lower temperature than the bulk liquid. As a result, the melting point depression is inversely proportional to the pore size. The technique is closely related to

that of the use of gas adsorption to measure pore sizes (Kelvin equation). This technique is particular case of the Gibbs equations (Josiah Willard Gibbs); the Kelvin equation is the constant temperature case, and the Gibbs-Thomson equation is the constant pressure case. To make a NMR measurement, a liquid is imbibed into the porous sample, the sample cooled until all the liquid is frozen, and then warmed slowly while measuring the quantity of the liquid melted. Thus, it is similar to DSC thermoporosimetry, but has higher resolution, as the signal detection does not rely on transient heat flows, and the measurement can be made arbitrarily slowly. It is suitable for measuring pore diameters in the range 2 nm–2 μm. Experimental results showed that the wet and dry porosity of the cement samples measured using these two different techniques are almost the same.

Table 2 Comparison of wet porosity with dry porosity

Core #	Wet Porosity (NMR)	Dry Porosity (air)
32	24.78%	24.19%
33	29.19%	29.30%
34	28.81%	29.68%
35	28.20%	28.93%
36	28.67%	27.97%

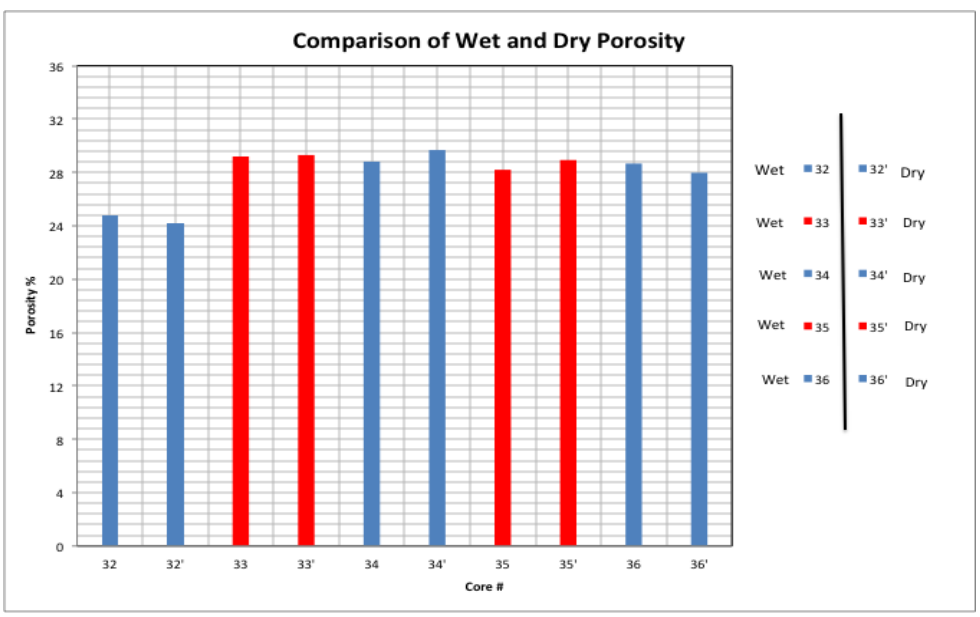

Fig. 4 Comparison of wet porosity with dry porosity

Total porosity of the cement samples were also measured using the low pressure pycnometer (LPP) technique. LPP is based on measuring the grain volume of finely crushed samples after removing free water. Once the bulk volume is determined the sample is ground into powder; it is carefully dried to remove free moisture and the volume of the powder (grains) is accurately determined. The difference between the bulk volume and grain volume is the measure of pore volume. Porosity measured using LPP technique (31.16%) was almost similar to porosity measured using AP608 technique (28.24%). This means that the total porosity of cement specimens is almost the same as connected porosity. In other words, most of the pores in the cement specimens are connected to each other.

SEM was used to study the different phases in the cement. Fig. 5 shows the back scattered SEM image of the cement surface at two different magnifications of 200X and 1000X. In these figures, white phase shows the unhydrated cement, light gray shows the CH phase, and dark gray shows the CSH phase. Prediction of molar concentration of CH and CSH of class H cement (Section A.1.6) shows that CH molar concentration is almost twice as CSH which shows good agreement with SEM experimental results. Light gray (i.e. CH) is approximately as twice as dark gray (i.e. CSH) in the SEM image.

A micro crack was observed in the SEM image. Therefore, it is preferred to use the coring technique for sample preparation. SEM image also shows the amount of unhydrated cement (white area in Fig 5). Prediction of maximum degree of hydration for class H cement (Section A.1.5) shows that the maximum hydration is about 60% which shows almost a good agreement with the amount of hydrated and unhydrated cement observed in SEM image in magnification of 1000X.

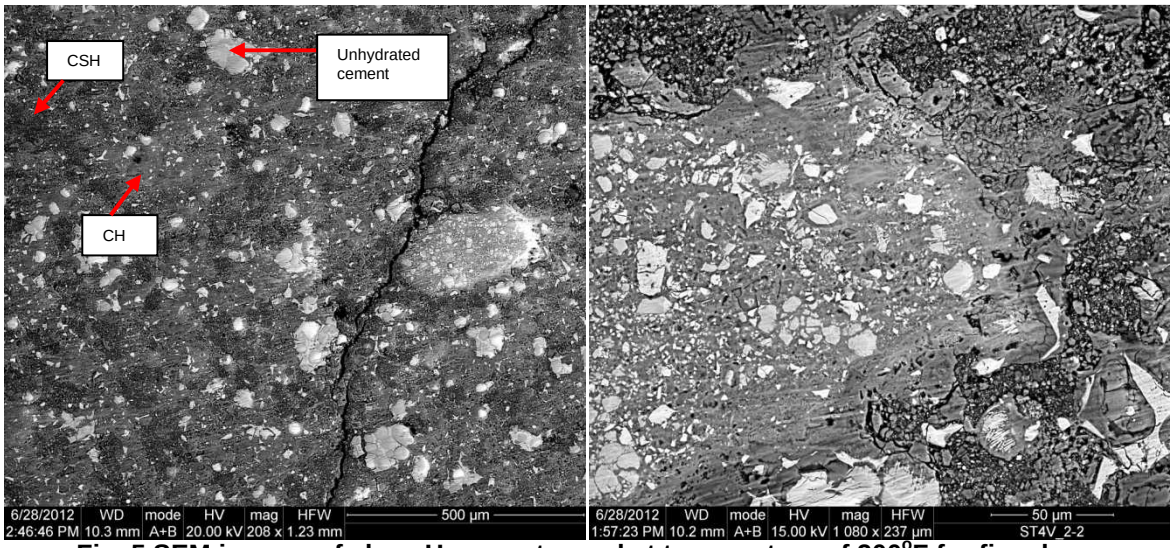

Fig. 5 SEM images of class H cement cured at temperature of 200°F for five days

During SEM imaging, XRF was also applied to analyze the amount of different elements in different phases observed in the SEM image (Figs. 6 through 8). XRF analysis results show that calcium is the dominant element in the cement. Different elements including Fe, Si, Mg, Na, O and Al can also be observed in the XRD pattern. Si is the second dominant element in the cement, which presents in CSH and unhydrated cement.

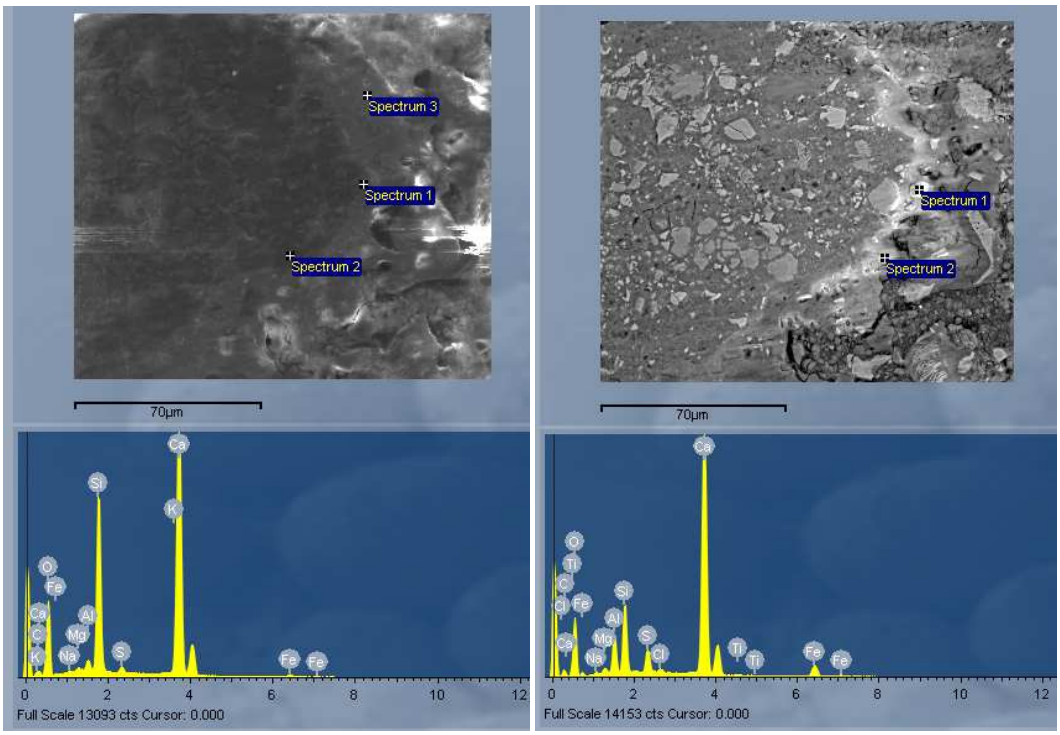

Fig. 6 XRF analysis of Core 28 (Left: spectrum 1, Right: spectrum 2)

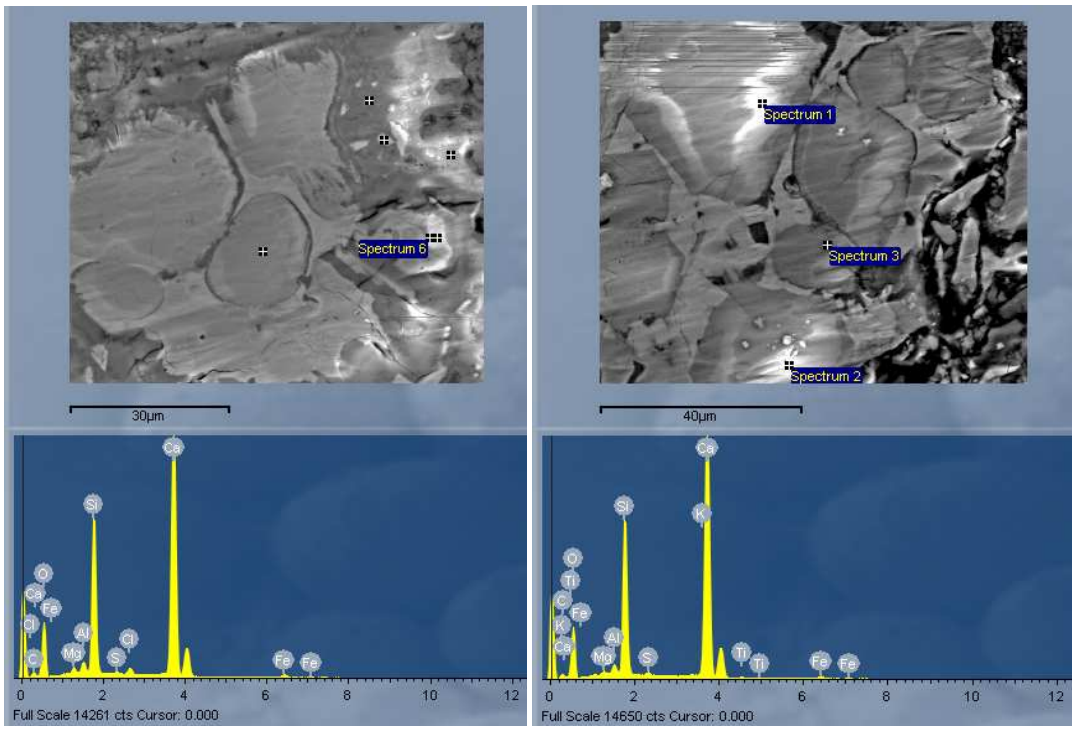

Fig.7 XRF analysis of Core 28 (Left: spectrum 6, Right: spectrum 3)

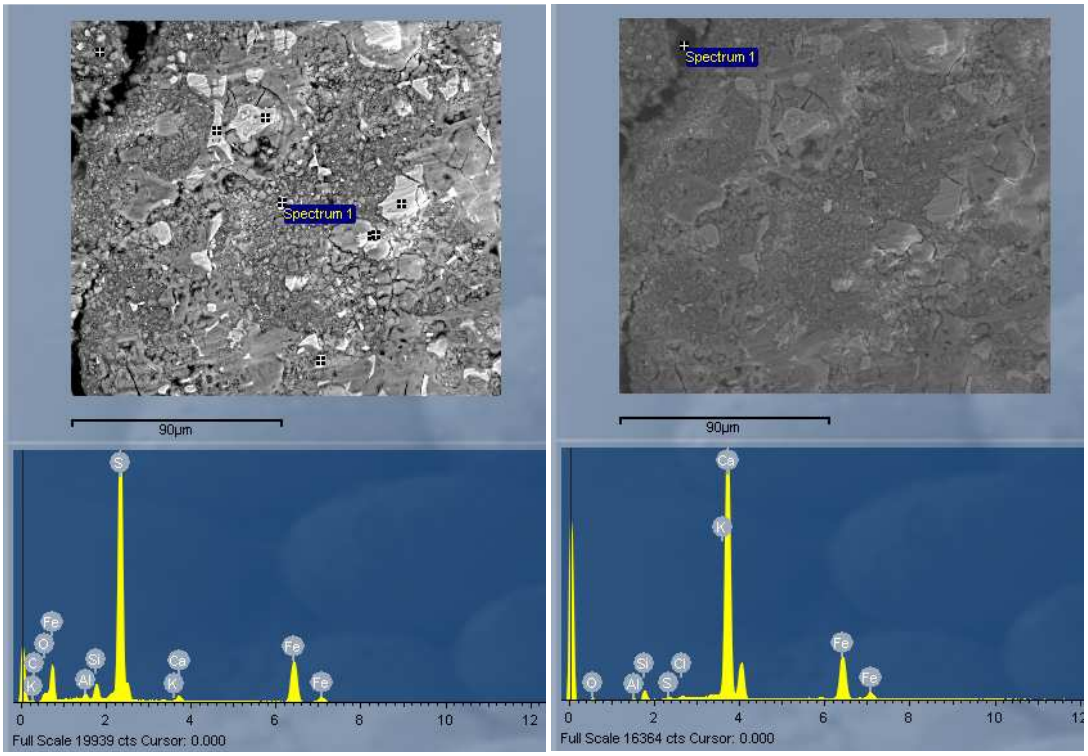

Fig.8 XRF analysis of Core 28 (Left: spectrum 1, Right: spectrum 1)

Fourier Transform Infra-Red (FTIR) spectroscopy was also used to study the applicability of this technique for studying the hydration process and also to qualitative and

quantitative detection of different phases in cement (Figs. 9 through 11). Three different samples were used for FTIR test as follow:

i. Hydrated cement with ashing (i.e. the powdered sample is kept where all the present organic content is removed and hence FTIR measurements)
ii. Hydrated cement without ashing
iii. Unhydrated cement sample (Class H cement powder before mixing with water)

FTIR spectrums of hydrated cement with and without ashing (Fig. 9 and 10 respectively) were almost similar to each other. FTIR spectrum of unhydrated cement (Fig. 11) was slightly different from the hydrated one. Experimental FTIR spectrums were compared with FTIR spectrum of well debris, $CaCO_3$ (Fig. 12), unexposed cement, and aged cement (Fig. 13). In general, the FTIR spectrums were less helpful for quantitative and qualitative analysis of cement. Therefore, the feasibility of other techniques such as XRD will be explored in future to fulfill the need of phase analysis.

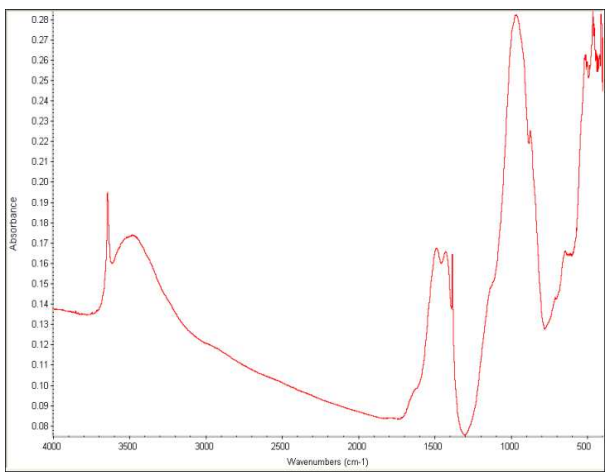

Fig. 9 FTIR spectra for hydrated cement sample with ashing

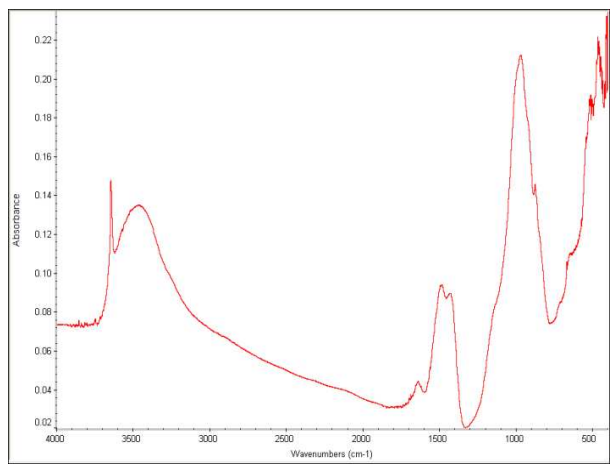

Fig. 10 FTIR spectra for hydrated cement sample without ashing

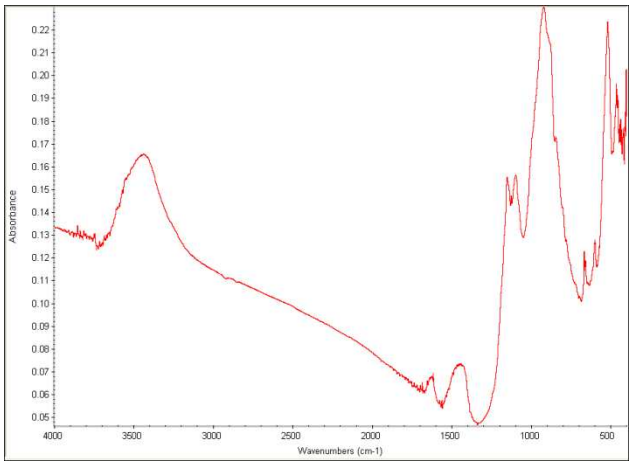

Fig. 11 FTIR spectra for unhydrated cement sample

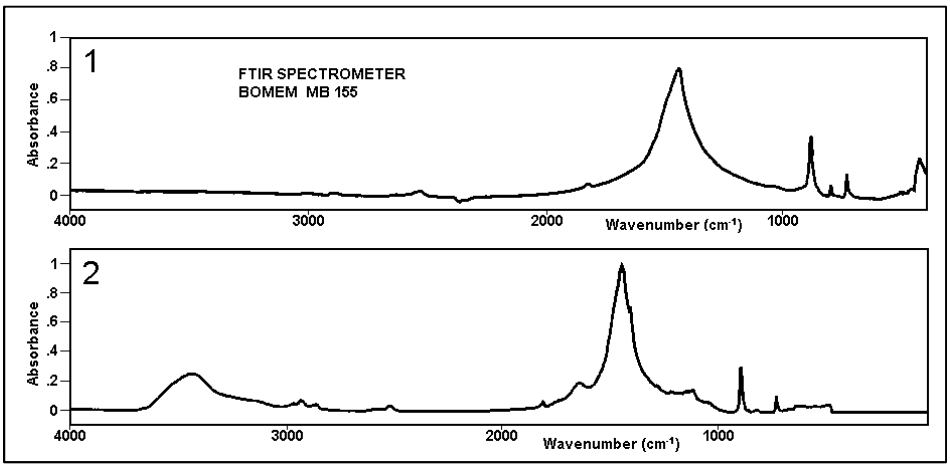

Fig. 12 FTIR spectra: 1) for well debris; and 2) for $CaCO_3$ (Krilov et al., 2000)

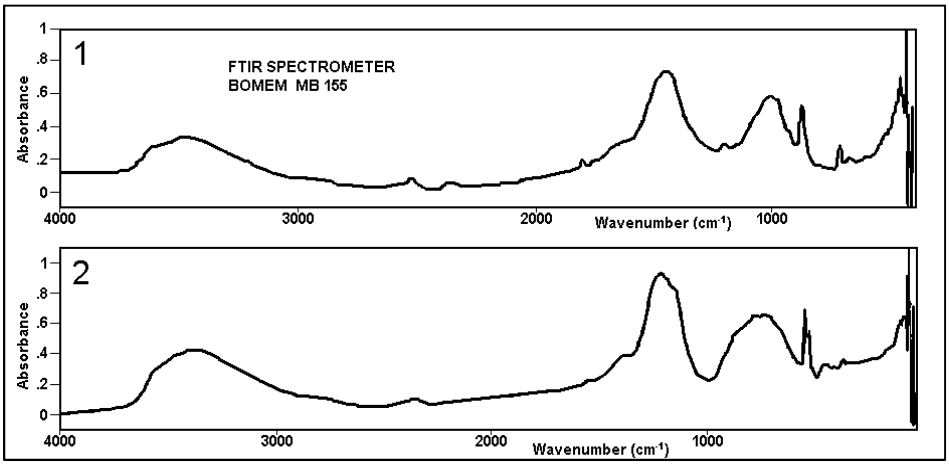

Fig. 13 FTIR spectra of cement: 1) before aging; and 2) after aging (Krilov et al., 2000)

In addition to the compositional analysis, unconfined compressive strength of four cement cores (Sample # 40, 42, 43, and 45) were measured. Compressive strength test results (Fig. 14a) for were fairly consistent for 1-inch long cores (Core # 40, 42 and 43). However, for 2-inch long core (Core # 45), measured compressive strength is slightly higher. Stress-strain graph of Core # 45 is shown in Fig. 14b. The stress-strain relationship is approximately linear. Elastic module of the core is found to be 500,000 psi.

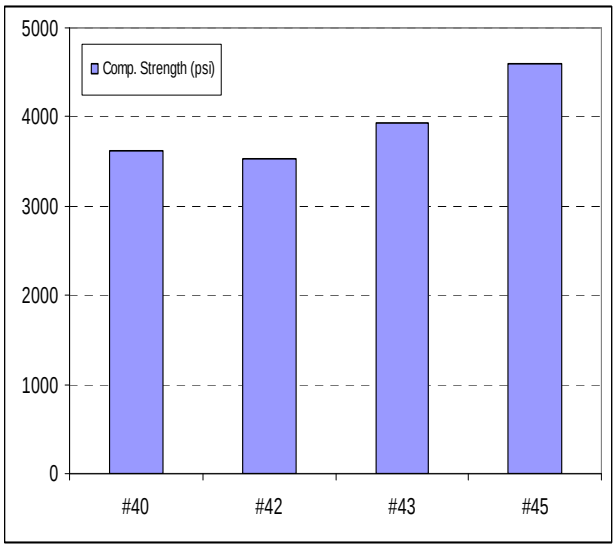

Fig. 14a Compressive strength cement cores

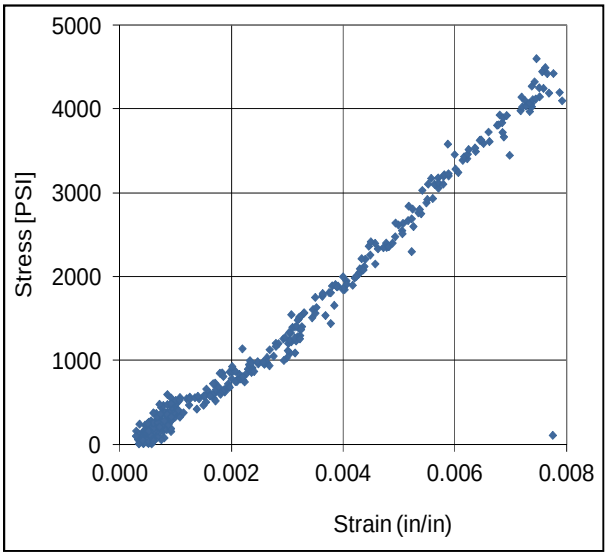

Fig. 14b Measured stress vs. strain for core #45

2.3 Experimental Studies on Corrosion of Tubulars (Task 3)

Searching for high-pressure recirculation pumps was continued. We are considering different options including using an injection cylinder as a pump, acquiring a custom-made pump or syringe type pump that meets the desired specifications. The design of the corrosion setup will be finalized after specifying the pump.

3. Planned Activities

- Aging experiments.
- Continue theoretical and modeling studies on cement and tubular degradation.
- Continue evaluating cement core preparation procedure.
- Designing of test setups to conduct tubular corrosion experiments.

4. Meeting and contacts

During this reporting period, we have made contacts with TAB members, Mr. Gunnar DeBruijn and Dr. Ashok Santra to discuss in detail cement slurry mixing procedure and formulations. Members recommend the use of API cement mixer for preparing the slurry. After the consultations, the following (Tables 2 through 5) cement slurries have been prepared using the API mixer to carry out the first aging experiments. In addition, TAB members pointed out the need of slow depressurization of the aging cell after aging the cement specimens. This is to minimize the development of micro cracks in the specimens because of quick expansion of the pore fluid.

Table 2 Cement Class H plus 35%silica and 100%fly ash

Material	Percent	Mass (g)	Specific Gravity	Volume (cc)
HEC	0.1% of water of filler	0.45	-	-
Cement	100%	860	3.14	273.9
Silica Fume	35% of cement	301	2.63	114.4
Fly Ash	100% of cement	860	2.63	327.0
Water for cement	38% cement	327	1.00	326.8
Water for Silica	38.5% silica	116	1.00	115.8
Water for Fly ash	38.5% fly ash	331	1.00	330.9
Total		**2795**		**1488.9**
Density (g/cc)	**1.88**			
Density (lbm/gal)	**15.66**			

Table 3 Cement Class H plus 35%silica

Material	Percent	Mass (g)	Specific Gravity	Volume (cc)
HEC	0.1% of water of filler	0.12	-	-
Cement	100%	860	3.14	273.9
Silica Fume	35% of cement	301	2.63	114.4
Fly Ash	100% of cement	0	2.63	0.0
Water for cement	38% cement	327	1.00	326.8
Water for Silica	38.5% silica	116	1.00	115.8
Water for Fly ash	38.5% fly ash	0	1.00	0.0
Total		**1604**		**831.0**
Density (g/cc)	**1.93**			
Density (lbm/gal)	**16.11**			

Table 4 Cement Class G+35%silica +100%fly ash

Material	Percent	Mass (g)	Specific Gravity	Volume (cc)
HEC	0.1% of water of filler	0.45	-	-
Cement	100%	860	3.14	273.9
Silica Fume	35% of cement	301	2.63	114.4
Fly Ash	100% of cement	860	2.63	327.0
Water for cement	44% cement	378	1.00	378.4
Water for Silica	38.5% silica	116	1.00	115.8
Water for Fly ash	38.5% fly ash	331	1.00	330.9
Total		**2846**		**1540.5**
Density (g/cc)	**1.85**			
Density (lbm/gal)	**15.42**			

Table 5 Cement Class G+35%silica

Material	Percent	Mass (g)	Specific Gravity	Volume (cc)
HEC	0.1% of water of filler	0.12	-	-
Cement	100%	860	3.14	273.9
Silica Fume	35% of cement	301	2.63	114.4
Fly Ash	100% of cement	0	2.63	0.0
Water for cement	44% cement	378	1.00	378.4
Water for Silica	38.5% silica	116	1.00	115.8
Water for Fly ash	38.5% fly ash	0	1.00	0.0
Total		**1655**		**882.6**
Density (g/cc)	**1.88**			
Density (lbm/gal)	**15.65**			

We also contacted Dr. Daniel Resasco from our Chemical Engineering department and Dr. Cornell from the University of Tulsa to explore the possibility of running XRD tests. Using XRD measurements, the compositional change occurring in the cement as a result of acid attack can be determined.

5. Project Expenditures

This section presents the project expenses during the months of June (Table 3) and the cumulative expenditures.

Table 3 Current and cumulative expenditures, June, 2012

No.	Budget Categories	Current Expenses	Cumulative Expenses
1	Salaries & Wages	$33,014.61	$59,585.99
2	Fringe Benefits	$11,494.95	$15,045.83
3	Project Materials	$604.60	$34,663.74
4	Travel	$139.31	$1,077.22
5	Conference Expenses	$0.00	$0.00
6	Other Direct Costs	$0.00	$305.38
7	Equipment	$4,818.44	$102,531.76
8	Space Rental	$0.00	$0.00
9	Indirect Cost	$22,626.74	$55,339.11
10	**Total**	**$72,698.65**	**$268,549.03**

Nomenclature

$\dot{\alpha}$	Normalized hydration rate
A_α	Chemical affinity
η_α	Permeability of the hydration products around the anhydrous cement
E_a	Apparent activation energy
R	Universal gas constant
T	Absolute temperature
α_u	Ultimate degree of hydration
α	Degree of hydration
Blaine	Fineness of cement particles
s(α, p)	Effect of applied hydrostatic pressure p
p	Hydrostatic pressure
R_p	Polarization Resistance
i_{corr}	Corrosion Current
B	Empirical polarization resistance constant
Y^*	Admittance representation
K_{mt}	Mass transfer coefficient
$[Fe^{2+}]_s$	Iron ion concentration on the metal surface
$[Fe^{2+}]_b$	Iron ion in the bulk solution
F	Faraday constant
K_{Fe}	Electrochemical reaction rate constant of iron ions
B	Transfer coefficient (the value of B is 0.5 for most of the reactions),
E_{corr}	Corrosion potential
E^o_{Fe}	Standard potential of iron at temperature T
K_1	First dissociation constant of Carbonic Acid
K_2	Second dissociation constant of Carbonic Acid
h	Plank's constant
ϑ	Frequency of vibration of complex
K	Boltzman's constant.
R_x	Reaction rate constant
$\Delta G^\#$	Gibbs free energy
i_o	Exchange current density
E_o	Equilibrium open circuit potential

References

Adsani, E., Shirazi, S.A. Shadley, J.R., Rybicki, E.F. 2006. Validation of Mass Transfer Coefficient Models used in Predicting CO_2 Corrosion in Vertical Two-Phase Flow in the Oil and Gas Production, Paper 06573, presented at the NACE Corrosion conference, Houston, TX.

Anderko, A. and Young, R. D. 1999. Simulation of CO_2/H_2S Corrosion Using Thermodynamic and Electrochemical Models, Paper No. 31, presented at the NACE CORROSION conference, Houston, TX.

Anderko, A. 2000. Simulation of $FeCO_3$/FeS Scale Formation Using Thermodynamic and Electrochemical Models, Paper No. 102, presented at the NACE CORROSION conference, Houston, TX.

Bentz, D.P. and Garboczi, E.J. 1992. Modeling the leaching of calcium hydroxide from cement paste: effects on pore space percolation and diffusivity, Materials and Structures, Volume 25, Number 9, 523-533, DOI: 10.1007/BF02472448.

Bentz, D.P., Garboczi, E.J., 1989. A digitized simulation model for microstructural development, in: S. Mindess (Ed.), Advances in Cementitious Materials, American Ceramic Society, Westville, Ohio, USA, pp. 211–226.

Bogue, R.H., 1947. The Chemistry of Portland Cement, Reinhold Publishing Corp., New York, USA.

Bonis, M. R. and Crolet, J. L. 1989. Basics of the Prediction of the Risks of CO_2 Corrosion in Oil and Gas Wells. Paper No. 466, presented at the NACE CORROSION conference, Houston, TX.

Chokshi, K., W. Sun, S. Nešić, 2005. Iron carbonate film growth and the effect of inhibition in CO_2 corrosion of mild steel, NACE International corrosion conference: Houston, TX.

Crolet, J. L., Bonis, M. R., 1991. Prediction of the Risks of CO2 Corrosion in Oil and Gas Well.SPE Production Engineering, Vol. 6, No. 4, p. 449.

Crolet, J.-L. and Bonis, M.R. 1991. Prediction of the Risks of CO2 Corrosion in Oil and Gas Well, SPE Prod. Eng. 6, p. 449.

Danielson, U., 1962. Heat of hydration of cement as affected by water–cement ratio, Paper IV-S7, Proceedings of the 4th International Symposium on the Chemistry of Cement, Washington DC, USA, pp. 519–526.

Dayalan, E., Vani, G., Shadley, J.R., Shirazi, S.A. and Rybicki, E.F. 1995. Modeling CO_2 corrosion of carbon steel in pipe flow, Paper No. 118, presented at the NACE corrosion conference.

Dayalan, E., de Moraes, F.D., Shadley, J.R., Shirazi, S.A., Rybicki, E.F., 1998. CO2 Corrosion Prediction in Pipe Flow Under $FeCO_3$ Scale-Forming Conditions, Paper no. 51, presented at the NACE CORROSION conference, Houston, TX.

de Waard, C.and Milliams, D.E., Corrosion 31 (1975): p. 131.

de Waard, C, Lotz, U., Milliams, D.E., Corrosion 47 (1991): p. 976.

de Waard, C, Lotz, U. and Dugstad, A. 1995. Influence of Liquid Flow Velocity on CO_2 Corrosion: A Semi-Empirical Model, Paper No. 128, presented at the NACE CORROSION conference, Houston, TX.

de Waard, C., Smith, L. and Craig, B.D. 2003. The Influence of Crude Oil on Well Tubing Corrosion Rates, Paper No. 03629, presented at the NACE CORROSION conference, Houston, TX.

Dugstad, A., Lunde, L. and Videm, K. 1994. Parametric Study of CO_2 Corrosion of Carbon Steel, Paper No. 14, presented at the NACE CORROSION conference, Houston, TX.

Epelboin, I., M. Keddam, and H. Takenouti, 1972. Use of impedance measurements for the determination of the instant rate of metal corrosion Journal of Applied Electrochemistry, 2: p. 71-79.

Fang, H., B. Brown, and S. Nešić, High salt, 2010. concentration effects on CO_2 corrosion and H_2S corrosion. NACE Intrnational corrosion conference, San Antonio, TX.

Fosbøl, P.L., Thomsen, K., Stenby, E. H., 2009. Improving mechanistic CO_2 corrosion Models.

Garber, J.D., Polaki, V., Adams, C. and Varanasi, N.R. 1998. Modeling Corrosion Rates in Non-Annular Gas Condensate Wells Containing CO_2, Paper No. 53, presented at the NACE CORROSION conference, Houston, TX.

Gartland, P.O. and Salomonsen, J. E. 1999. A Pipeline Integrity Management Strategy Based on Multiphase Fluid Flow and Corrosion Modelling, Paper No. 622, prestned at CORROSION conference, Houston, TX.

Gartland, P.O., Johnsen, R. and Øvstetun, I., 2003. Application of Internal Corrosion Modeling in the Risk Assessment of Pipelines, Paper No. 03179, presented at the NACE CORROSION conference, Houston, TX.

Gray, L.G.S., B.G. Anderson, M.J. Danysh, P.G. Tremaine, 1989. Mechanism of carbon steel corrosion in brines containing dissolved carbon dioxide at pH 4, NACE International corrosion conference: Houston, TX.

Gunaltun, Y. M., 1996. Combining research and field data for corrosion rate prediction. Paper No. 27, presented at the NACE CORROSION conference, Houston, TX.

Halvorsen, A.M.K., Søntvedt, T., 1999. CO_2 Corrosion Model for Carbon Steel Including a Wall Shear Stress Model for Multiphase Flow and Limits for Production Rate to Avoid Mesa Attack, Paper No. 42, presented at the NACE CORROSION conference, Houston, TX.

Hassani, S., Roberts K.P., Shirazi S.A., Shadley J.R., Rybicki E.F., Joia C., 2011. Flow Loop Study of Chloride Concentration Effect on Erosion, Corrosion and Erosion-Corrosion of carbon Steel in CO_2 Saturated Systems, NACE International corrosion conference, Houston, TX.

Hedges, B. Chapman, R., Harrop, D., Mohammed, I., Sun, Y., 2005. A Prophetic CO_2 Corrosion Tool - But When is it to be Believed?, Paper No. 05552, presented at the NACE CORROSION conference, Houston, TX, April 3 - 7.

Heidersbach, R., 2011. Metallurgy and Corrosion Control in Oil and Gas Production. Hoboken, NJ: Wiley.

High, M.S., Wagner, J. and Natarajan, S. 2000. Mechanistic Modeling of Mass Transfer in the Laminar Sublayer in Downhole Systems, Paper No. 62, presented at the NACE CORROSION conference, Houston, TX.

Hoffmeister, 2005. Modeling of H_2S Corrosion by Coupling of Phase and Polarization Behavior, Paper No. 5476, presented at the NACE CORROSION conference, Houston, TX, April 3 - 7.

Hoffmeister, 2007, Modeling the Effect of Chloride Content on H_2S Corrosion by Coupling of Phase and Polarization Behavior, Paper No. 7501, presented at the NACE CORROSION conference, Nashville, TN, March 11 – 15.

Hudak, P.F. and D.J. Wachal, 2001. Effects of brine injection wells, dry holes, and plugged oil/gas wells on chloride, bromide, and barium concentrations in the Gulf Coast Aquifer, southeast Texas, USA. Environment International, 26(7-8): p. 497-503.

Jacquemet,J., Pironon, J., Lagneau, V., Saint-Marc, J., 2012. Armouring of well cement in H_2S–CO_2-saturated brine by calcite coating–Experiments and numerical modeling. Applied Geochemistry 27. 782–795

Jepson, W.P., Kang, C., Gopal, M. and Stitzel, S. 1997. Model for Sweet Corrosion in Horizontal Multiphase Slug Flow, Paper No. 11, presented at the NACE CORROSION conference, Houston, TX.

John, R.C., Jordan, K. G., Young, A. L., Kapusta, S. D. and Thompson, W. T. 1998. SweetCor: An Information System for the Analysis of Corrosion of Steels by Water and Carbon Dioxide, Paper No. 20, presented at the NACE CORROSION conference, Houston, TX.

Keienburg, R.R., 1976. Particle Size Distribution and Normal Strength of Portland Cement, PhD Thesis, Karlsruhe University, Germany.

Kvarekval. J. and Videm, K., 1995. Corrosion of Carbon Steel in Carbon Dioxide-Saturated Solutions Containing Small Amounts of Hydrogen Sulfide. NACE international, April.

Lerch, W. Ford, C.L., 1948. Long-term study of cement performance in concrete: chapter 3. Chemical and physical tests of the cements, ACI Journal 19 (8) 745–795.

Lin, F., Meyer, C., 2009. Hydration kinetics modeling of Portland cement considering the effects of curing temperature and applied pressure, Cement and Concrete Research 39, 255–265.

McMahon, A.J., Paisley, D.M.E., 1997. Corrosion Prediction Modelling—A Guide to the Use of Corrosion Prediction Models for Risk Assessment in Oil and Gas Production and Transportation Facilities, Report no. ESR.96.ER.066 (Sunbury: BP International)

Millero, F., Huang, F., Graham, T., Pierrot, D., 2007, The dissociation of carbonic acid in NaCl solutions as a function of concentration and temperature, *Geochimica et Cosmochimica Acta* 71 pp. 46-55

Nesic, S., Postlethwaite, J., Olsen, S., 1996. An Electrochemical Model for Prediction of Corrosion of Mild Steel in Aqueous Carbon Dioxide Solutions. Corrosion, Vol. 52, No. 4, p. 280.

Nesic, S., Nordsveen, M., Nyborg, R., Stangeland, A., 2003. A Mechanistic Model for CO_2 Corrosion with Protective Iron Carbonate Films - Part 2: A Numerical Experiment. Corrosion, Vol. 59, No. 6, pp. 489-497.

Nesic, S., Li, H., Huang, J., Sormaz, D., 2009. An Open Source Mechanistic Model for CO_2 / H_2S Corrosion of Carbon Steel, NACE corrosion conference, Paper No. 9572

Nešić, S. 2007. Key issues related to modeling of internal corrosion of oil and gas pipelines, Corrosion Science, Vol. 49, Issue 12, December 2007, Pages 4308–4338.

Nordsveen, M., Nesic, S., Nyborg, R., Stangeland, A., 2003. A Mechanistic Model for CO_2 Corrosion with Protective Iron Carbonate Films - Part 1: Theory and Verification. Corrosion, Vol. 59, No. 5, pp. 443-456.

NORSOK Standard no. M-506. 1998. CO2 Corrosion Rate Calculation Model. Norwegian Technology Standards Institution, http://www.nts.no/norsok

Nyborg, R. Dugstad, A., 2003. Understanding and Prediction of Mesa Corrosion Attack, Paper No. 3642, presented at the NACE CORROSION conference, San Diego CA, March.

Nyborg, R., 2006. Field Data Collection, Evaluation and Use for Corrosivity Prediction and Validation of Models, Part II: Evaluation of Field Data and Comparison of Prediction Models, Paper no. 06118, NACE CORROSION conference, Houston, TX.

Nyborg, R., 2009. Guidelines for prediction of CO2 corrosion in oil and gas production systems, Material Technology, IFE, Kjeller, ISBN 978-82-7017-791-2.

Nyborg, R. 2010. CO2 Corrosion Models for Oil and Gas Production Systems, Paper No 10371, presented at the NACE corrosion conference, March 14 - 18, San Antonio, TX.

Perkins, R.S., Fang, C.S., Garber, J. D., Singh, R. K., 1996. Predicting Tubing Life in Annular-Flow Gas Condensate Wells Containing Carbon Dioxide, Corrosion, Vol. 52, No. 10, p. 801.

Pots, B.F.M., 1995. Mechanistic Models for the Prediction of CO_2 Corrosion Rates under Multi-Phase Flow Conditions, Paper No. 137, NACE CORROSION conference, Houston, TX.

Pots, B.F.M., John, R.C., Rippon, I.J., Thomas, J.S., Kapusta, S. D., Girgis, M. M. and Whitham, T. 2002. Improvements on de Waard - Milliams Corrosion Prediction and Applications to Corrosion Management, Paper No. 02235, presented at the NACE CORROSION conference, Houston, TX.

Pots, B.F.M. and Kapusta, S. D., 2005. Prediction of Corrosion Rates of the Main Corrosion Mechanisms in Upstream applications, Paper No. 05550, presented at the NACE CORROSION conference, Houston, TX.

Ramachandran, S., Ward M. B., and Bartrip, K. A., 2002. Molecular Modeling of Corrosion of Iron in H2S Environments, Paper No. 2240, presented at the NACE corrosion conference, April 7 - 11, Denver, CO.

Ramirez, M. and Ruiz, A.,1998. The Effect of Small Amounts of H_2S on CO_2 Corrosion of a Carbon Steel. NACE international.

Roberge, P.R., 1999. Handbook of Corrosion Engineering. New York: McGrow-Hill.

Ropital, F., 2010. Corrosion and degradation of metallic materials: Understanding of the phenomena and applications in petroleum and process industries.

Sangita, K. A. and Srinivasan, S., 2000. An Analytical Model to Experimentally Emulate Flow Effects in Multiphase CO2/H2S Systems. Paper No. 58, presented at the NACE CORROSION conference, Houston, TX.

Silva, C.A.R., X. Liu, and F.J. Millero, 2002. Solubility of Siderite in NaCl Solutions. Journal of Solution Chemistry, 31(2): p. 97-108.

Smith S. N., Pacheco, J.L., 2002, Prediction of Corrosion in Slightly Sour Environment, Paper No. 2241, presented at the NACE International corrosion conference, Houston TX.

Smith, L. and de Waard, C. 2005. Corrosion Prediction and Materials Selection for Oil and Gas Producing Environments, Paper No. 05648, presented at the NACE CORROSION conference, Houston, TX.

Srinivasan, S. and Kane, R. D., 1996. Prediction of Corrosivity of CO_2/H_2S Production environments. Paper No. 11, presented at the NACE CORROSION conference, Houston, TX.

Srinivasan S. and Kane, R. D. 2003. Critical Issues in the Application and Evaluation of a Corrosion Prediction Model for Oil and Gas Systems. Paper No. 03640, presented at the NACE CORROSION conference, Houston, TX.

Srinivasan, S., Kane, R.D., 1996. Prediction of Corrosivity of CO_2/H_2S Production Environments, Paper No. 11, presented at the NACE CORROSION conference, Houston, TX.

Sun, W., Nesic, S. 2007. A Mechanistic Model of H_2S Corrosion of Mild Steel, Paper No. 7655, presented at the NACE corrosion conference, March 11 - 15, Nashville, TN.

Sun, W., Nesic, S. 2008. A Mechanistic Model of Uniform Hydrogen Sulfide/Carbon Dioxide Corrosion of Mild Steel, Corrosion Journal, Vol. 65. No, 5.

Sun, W., S. Nesic, and R.C. Woollam, 2009. The effect of temperature and ionic strength on iron carbonate ($FeCO_3$) solubility limit. Corrosion Science, 51(6): p. 1273-1276.

Schmitt, G. and B. Rothmann, 1977. Corrosion Mechanism of Unalloyed Steel in Oxygen-Free Carbon Dioxide Solutions - 1. Untersuchungen Zum Korrosionsmechanismus Von Unlegiertem Stahl In Sauerstoffreinen Kohlensaeureloesungen - 1. Kinetik Der Wasserstoffabscheidung., 28(12): p. 816-822.

Shoesmith, D.W., Taylor, P., Bailey, M.G., Owen, D.G., 1980. The formation of ferrous monosulfide polymorphs during the corrosion of iron by aqueous hydrogen sulfide at 21 C, J. Electrochem. Soc. 127, 1007–1015.

Taplin, J.H., 1969. A method for following hydration reaction in Portland cement paste, Australian Journal of Applied Sciences 10 329–345.

Uhlig, H.H.a.R.W.R., 1985. Corrosion and corrosion control: An introduction to corrosion science and engineering. 4th ed. Hoboken, NJ: John Wiley & Sons.

Wang, S., K. George, S. Nešić, 2004. High pressure CO_2 corrosion electrochemistry and the effect of acetic acid, NACE International corrosion conference: Houston, TX.

Zhang, G.A. and Y.F. Cheng, 2009. Electrochemical corrosion of X65 pipe steel in oil/water emulsion. Corrosion Science, 51(4): p. 901-907.

Zhang, R., Gopal, M. and Jepson, W.P. 1997. Development of a Mechanistic Model for Predicting Corrosion Rate in Multiphase Oil/Water/Gas Flows, Paper No. 601, presented at the NACE CORROSION conference, Houston, TX.

Zhou, Q., Beaudoin, J.J., 2003. Effect of applied hydrostatic stress on the hydration of Portland cement and C_3S, Advances in Cement Research 15 (1) 9–16

Appendix A

Cement Hydration Modeling

Summary

Cement hydration modeling is essential to predict the amount of calcium presents in the CH and CSH phase of cement after curing and before aging. Calcium concentration in the solid phase (matrix) is necessary to predict the degradation depth, mechanical properties, and permeability of the cement using degradation models.

The rate and degree of cement hydration depends on cement composition, water-cement ratio, temperature, pressure, and cement fineness. Results obtained from a recent hydration model proposed by Lin and Meyer 2009 showed a good agreement with experimental data for seven different types of cement. The model is applied to predict the hydration degree of cement class H and G used in this project at two different temperatures. Maximum degree of hydration for class H and G is about 60%, which happens after 100 hours of curing in temperature of 200°F. Therefore, sample curing for more than 4 days at temperature of 200°F is sufficient to get the maximum possible hydration.

During this investigation, samples will be cured for 5 days at temperature of 200ºF. The hydration model provides the free (unhydrated) water remained after hydration, which is needed to predict the cement porosity after curing. Porosity prediction for cement class H cured for five days at temperature of 200°F is approximately 26% which showed a good agreement with experimental data (25-30%). Porosity prediction for cement class G cured for five days at temperature of 200°F was about 31%. Higher porosity for class G in comparison with class H is related to the higher water-cement ratio of class G cement. Porosity of sample after curing and before aging is used in leaching model to predict the degradation depth, mechanical properties, and permeability of the cement.

Adding silica fume to the cement affects the amount of CH and CSH in cement. Silica reacts with about 25% of free CH and produces CSH. Therefore, silica decreases the amount of CH and increases the amount of CSH.

A.1. Cement Hydration Modeling

Portland cement contains four crystalline compounds that hydrate to form a rigid structure. These compounds are: i) Tricalcium Silicate: $3CaO.SiO_2$ (C_3S, main contributor to the cement strength); ii) Dicalcium Silicate: $2CaO.SiO_2$ (C_2S, provides long term strength); iiI) Tricalcium Aluminate: $3CaO.Al_2O_3$ (C_3A, promote rapid hydration of cement); iv) Tetracalcium

Aluminoferrite: $4CaO.Al_2O_3.Fe_2O_3$ (C_4AF). During cement hydration, the main reaction products formed are tobermorite gel ($3CaO.2SiO_2.3H_2O$), which is known as calcium silicate hydrate (CSH) phase and the portlandite/calcium hydroxide (CH).

$$2(3CaO.SiO_2) + 6H_2O \rightarrow 3CaO.2SiO_2.3H_2O + 3Ca(OH)_2 \quad \text{(A.1)}$$

$$2(2CaO.SiO_2) + 4H_2O \rightarrow 3CaO.2SiO_2.3H_2O + Ca(OH)_2 \text{ (slow reaction)} \quad \text{(A.2)}$$

$$3CaO.Al_2O_3 + 12H_2O + Ca(OH)_2 \rightarrow 3CaO.Al_2O_3.Ca(OH)_2.12H_2O \text{ (fast reaction)} \quad \text{(A.3)}$$

$$3CaO.Al_2O_3 + 10H_2O + CaSO_4.2H_2O \rightarrow 3CaO.Al_2O_3.CaSO_4.12H_2O \quad \text{(A.4)}$$

$$4CaO.Al_2O_3.Fe_2O_3 + 10H_2O + 2CaO.H_2O \rightarrow 6CaO.Al_2O_3.Fe_2O_3.12H_2O \text{ (slow)} \quad \text{(A.5)}$$

The hydration of cement causes heat generation, strength development and shrinkage. A thorough understanding of chemical, physical and mechanical processes is important for cement hydration modeling.

Lin and Meyer (2009) developed a hydration kinetics model for Portland cement which is applicable for elevated temperatures and high pressure conditions. The model is based on thermodynamics analysis of multiphase porous media which was first proposed by Ulm and Coussy (1995). This model considers the effects of chemical composition and fineness of cement, water–cement ratio, curing temperature, and applied pressure the analysis. The model was calibrated using the experimental data obtained from eight different Portland cements. In addition, correlations were developed to relate model parameters and cement composition.

CH and CSH concentration in cement is needed for predicting the leaching rate, degradation depth, porosity, permeability, and mechanical properties of well cement. Degree of hydration has to be predicted in order to calculate the CH and CSH concentrations in cement. In this project, the model developed by Lin and Meyer (2009) is used to predict the hydration level in cement specimens. Applying the model, degree of hydration can be predicted as a function of influential parameters such as chemical composition of cement (i.e. C_3S, C_2S, C_3A, and C_4AF weight fraction), temperature, water-cement ratio, pressure, and fineness of cement. In this study, the effects of different influential parameters on the degree of hydration are investigated.

A.1.1 Effects of Influential Parameters on Hydration Rate

A.1.1.1 Chemical Composition of Cement

The composition of cement is one of the most important influential parameters that affects degree of cement hydration. Because of different reaction rates of the clinker phases (i.e. C_3S, C_2S, C_3A, and C_4AF) and their interactions, it is generally accepted that the so-called degree of hydration of cement is just an overall and approximate measure.

A.1.1.2 Water-Cement Ratio

Experimental results have shown that a higher water–cement ratio leads to a higher hydration rate after the middle period of hydration, but only has a small effect on the hydration rate in the early stage. The water–cement ratio also determines the ultimate degree of hydration (α_u). Theoretically, a water–cement ratio of about 0.4 is sufficient for the complete hydration of cement (i.e. α_u=1.0). The hydration products around the anhydrous cement particles prevent further hydration if there is insufficient amount of free water in the macro-pores.

A.1.1.3 Fineness

The finer cement particles lead to the higher α_u, and consequently the higher the hydration rate. Bentz and Haecker (1989) also found that at low water–cement ratios, the influence of cement fineness on α_u diminishes. A finer cement, or cement with a larger surface area, provides a larger contact area with water and hence causes a higher hydration rate. Also, at the same degree of hydration, a larger surface area corresponds to a smaller thickness of hydration products around the anhydrous cement particles, which increases the ultimate degree of hydration. Apart from fineness, the particle size distribution of cement influences the hydration rate.

A.1.1.4 Curing Temperature

The effects of curing temperature on hydration kinetics have been shown to be twofold. On the one hand, the reaction rate $\dot{\alpha}$ increases with the increase in temperature. On the other hand, the density of hydration products at higher temperature is higher, which slows down the permeation of free water through the hydration products. Therefore, during the late period, the hydration rate is lower at elevated temperature and the ultimate degree of hydration may thus also be lower.

A.1.1.5 Pressure

Zhou and Beaudoin (2003) found that applied hydrostatic pressure increases the hydration rate of Portland cement; however, it has only a negligible effect on the pore structure of hydration products when different cement pastes at similar degrees of hydration are compared. This finding is important since it implies that the density of the hydration products is not considerably affected by the applied hydrostatic pressure, at least not up to 6.8 MPa, which is the pressure they used in the investigation.

A.1.2 Cement Hydration Mechanism

Van Breugel (1991) suggested three main stages (early, middle and late periods) of cement hydration. The early stage includes a short period of rapid chemical dissolution, termed as the pre-induction period, which is followed by a dormant stage, which lasts for several hours. After that, cement hydration enters the middle stage that can last for 24 to 48 hours, in which ions transport to and from the surfaces of anhydrous cement particles through gradually growing layers of hydration products. During the late stage, which is the longest and dominant one, the reaction is totally diffusion-controlled. The free water in macro-pores diffuses through the hydration products formed around the anhydrous cement core, making further reactions possible. It was reported that cement hydration follows two different mechanisms (phase boundary and diffusion controlled mechanisms) at different stages. During the early and middle periods, the phase boundary mechanism prevails, while in the late period, the diffusion-controlled reaction dominates. However, it is very difficult to define a clear or definite boundary between the two mechanisms.

The hydration model presented by Lin and Meyer (2009) is a unified model. It considers the phase boundary mechanism as a special case of the diffusion-controlled reaction when the layers of hydration products around the anhydrous cement cores are very thin. The mechanisms of cement hydration are then unified to be the diffusion-controlled one. Cement hydration is interpreted as a chemical reaction in which the free water in the macro-pores combines as a reactant phase with the anhydrous cement and becomes the chemically bound water as a product phase, and the dominant mechanism of the reaction kinetics is the diffusion of free water through layers of hydration products.

A.1.3 Cement Hydration Model Formulation

The normalized hydration rate $\dot{\alpha}$ can be written as:

$$\dot{\alpha} = A_\alpha \eta_\alpha \exp\left(-\frac{E_a}{RT}\right) \exp\left(-\frac{E_a}{293R}\right) \quad \text{(A.6)}$$

where A_α is chemical affinity, η_α represents the permeability of the hydration products around the anhydrous cement and can be calculated using Eqs. (A.17) through (A.22), E_a is the apparent activation energy (Eq. A.23), R is the universal gas constant, and T is the absolute temperature. The normalization in Eq. (A.6) ensures that the material constants of the model can be obtained from experimental results at room temperature and will not vary considerably for different values of activation energy.

The chemical affinity A_α is expressed as:

$$A_\alpha\left(\alpha, \frac{W}{C}, Blaine, P\right) = k\left(\frac{A_o}{k\alpha_u} + \alpha\right).(\alpha_u - \alpha).S(\alpha, P) \quad \text{(A.7)}$$

where the constants k can be represented by a nonlinear function (Eq. A.8) of mass fractions of C_3S, C_2S, and C_3A (Bogue, 1947). A_o can be calculated using Eqs. (A.9) and (A.10). α_u is ultimate degree of hydration which can be calculated using Eq.(A.11) through (A.14). α is degree of hydration. Blaine represents the fineness of cement particles. The function s(α, p) represents the effect of applied hydrostatic pressure p which can be calculated using Eq. (A.16).

$$k = 0.56\left(P_{C_3S}\right)^{-0.206}\left(P_{C_2S}\right)^{-0.128}\left(P_{C_3A}\right)^{0.161} \quad \text{(A.8)}$$

$$A_o = \frac{\acute{A}_o \times Blaine}{350} \quad \text{(A.9)}$$

$$\acute{A}_o = -0.0767 P_{C_4AF} + 0.0184 \quad \text{(A.10)}$$

$$\alpha_u = \alpha_{u,293} exp[-0.00003(T - 293)^2.SGN(T - 293)] \quad \text{(A.11)}$$

$$\alpha_{u,293} = \frac{\beta_1(Blaine) \times \frac{W}{C}}{\beta_2(Blaine) + \frac{W}{C}} \leq 1.0 \quad \text{(A.12)}$$

$$\beta_1(Blaine) = \frac{1}{9.33\left(\frac{Blaine}{100}\right)^{-2.82} + 0.38} \quad \text{(A.13)}$$

$$\beta_2(Blaine) = \frac{Blaine-220}{147.78+1.656(Blaine-220)} \quad \text{(A.14)}$$

Equations (A.13) and (A.14) are valid for Blaine ≥ 270 m^2/kg. When Blaine < 270 m^2/kg, β_1 and β_2 are assumed to be constant.

$$SGN(T-293) = \begin{cases} 1, when\ T \geq 293K \\ -1, when\ T < 293K \end{cases} \quad \text{(A.15)}$$

$$S(\alpha, P) = exp\left\{0.02\left(\frac{P}{P_{atm}} - 1\right)^{0.07}\left[\frac{\alpha}{\alpha_u} - 1.5\left(\frac{\alpha}{\alpha_u}\right)^2 + 0.4\right]\right\} \quad \text{(A.16)}$$

Free water permeability can be written as the following correlation.

$$\eta_\alpha = exp(-n\alpha) \quad \text{(A.17)}$$

In which “n” is a parameter that depends on curing temperature, degree of hydration, and fineness of cement. The value of “n” can be determined using Equations (A.18) through (A.22).

$$n = n_o f_1(Blaine, \alpha).f_2(T, \alpha) \quad \text{(A.18)}$$

$$n_o = 10.945\left(P_{C_3S}\right) + 11.25\left(P_{C_2S}\right) - 4.1\left(P_{C_3A}\right) - 0.892 \quad \text{(A.19)}$$

$$f_1(Blaine, \alpha) = 1 + (1-\alpha)^2.Ln\left(\frac{350}{Blaine}\right) \quad \text{(A.20)}$$

$$f_2(T, \alpha) = \left(\frac{V_{293}}{V(T)}\right)^{10(\alpha)^4} \quad \text{(A.21)}$$

$$\frac{V_{293}}{V(T)} = exp(28 \times 10^{-6}(T-293)^2) \quad \text{(A.22)}$$

Apparent activation energy (E_a) can be calculated using the Eq. (A.23) as a function of C_3A, and C_4AF weight fractions and Blaine fineness of cement.

$$E_a = 22100 \times \left(P_{C_3A}\right)^{0.3}\left(P_{C_4AF}\right)^{0.25}(Blaine)^{0.35} \quad \text{(A.23)}$$

In general, hydration degree can be written as a function of chemical composition of cement (i.e. C_3S, C_2S, C_3A, and C_4AF weight fraction), temperature, water-cement ratio, pressure, and fineness of cement (Eq. A.24).

$$\frac{d\alpha}{dt} = \dot{\alpha} = A_\alpha \eta_\alpha \exp\left(-\frac{E_a}{RT}\right)\exp\left(-\frac{E_a}{293R}\right)$$

$$= 0.56\left(P_{C_3S}\right)^{-0.206}\left(P_{C_2S}\right)^{-0.128}\left(P_{C_3A}\right)^{0.161}\left(\frac{A_o}{0.56\left(P_{C_3S}\right)^{-0.206}\left(P_{C_2S}\right)^{-0.128}\left(P_{C_3A}\right)^{0.161}\dfrac{\dfrac{1}{9.33\left(\frac{Blaine}{100}\right)^{-2.82}+0.38}\times\frac{W}{C}}{\dfrac{Blaine-220}{147.78+1.656(Blaine-220)}+\frac{W}{C}}\times exp[-0.00003(T-293)^2]}\right.$$

$$\left.+\alpha\right).\left(\frac{\dfrac{1}{9.33\left(\frac{Blaine}{100}\right)^{-2.82}+0.38}\times\frac{W}{C}}{\dfrac{Blaine-220}{147.78+1.656(Blaine-220)}+\frac{W}{C}}\times exp[-0.00003(T-293)^2]\right)$$

$$\left.-\alpha\right).exp\left\{0.02\left(\frac{P}{P_{atm}}-1\right)^{0.07}\left[\frac{\alpha}{\dfrac{\dfrac{1}{9.33\left(\frac{Blaine}{100}\right)^{-2.82}+0.38}\times\frac{W}{C}}{\dfrac{Blaine-220}{147.78+1.656(Blaine-220)}+\frac{W}{C}}\times exp[-0.00003(T-293)^2]}-1.5\left(\frac{\alpha}{\dfrac{\dfrac{1}{9.33\left(\frac{Blaine}{100}\right)^{-2.82}+0.38}\times\frac{W}{C}}{\dfrac{Blaine-220}{147.78+1.656(Blaine-220)}+\frac{W}{C}}\times exp[-0.00003(T-293)^2]}\right)^2\right.\right.$$

$$\left.\left.+0.4\right]\right\}exp\left(-\left[\left\{10.945\left(P_{C_3S}\right)+11.25\left(P_{C_2S}\right)-4.1\left(P_{C_3A}\right)-0.892\right\}\left\{1\right.\right.\right.$$

$$\left.\left.+(1-\alpha)^2.Ln\left(\frac{350}{Blaine}\right)\right\}.\left(exp(28\times10^{-6}(T-293)^2)\right)^{10(\alpha)^4}\right]\alpha\right)exp\left(-\frac{22100\times\left(P_{C_3A}\right)^{0.3}\left(P_{C_4AF}\right)^{0.25}(Blaine)^{0.35}}{RT}\right)\exp\left(-\frac{22100\times\left(P_{C_3A}\right)^{0.3}\left(P_{C_4AF}\right)^{0.25}(Blaine)^{0.35}}{293R}\right)$$

……..….(A.24)

A.1.4 Model Validation

Figures A.1 through A.4 compare model predictions with published experimental measurements (Lerch and Ford 1948, Keienburg, 1976, Danielson, 1962, Taplin, 1969). Seven different cements shown in Table A.1 are used to validate the model. A satisfactory agreement is found between the model and experimental measurements.

Table A.1 Cement composition and the corresponding material constants

	Bogue Composition				
Cement ID#	C_3S	C_2S	C_3A	C_4AF	Blaine Fineness (m^2/kg)
#A (Lerch and Ford 1948)	0.514	0.226	0.111	0.079	372
#B (Lerch and Ford 1948)	0.416	0.344	0.054	0.132	314
#C (Lerch and Ford 1948)	0.600	0.135	0.089	0.081	564
#D (Lerch and Ford 1948)	0.240	0.515	0.049	0.116	360
#E (Keienburg, 1976)	0.717	0.059	0.090	0.100	350
#F (Danielson, 1962)	0.567	0.172	0.067	0.079	312
#H (Taplin, 1969)	0.414	0.340	0.098	0.075	312

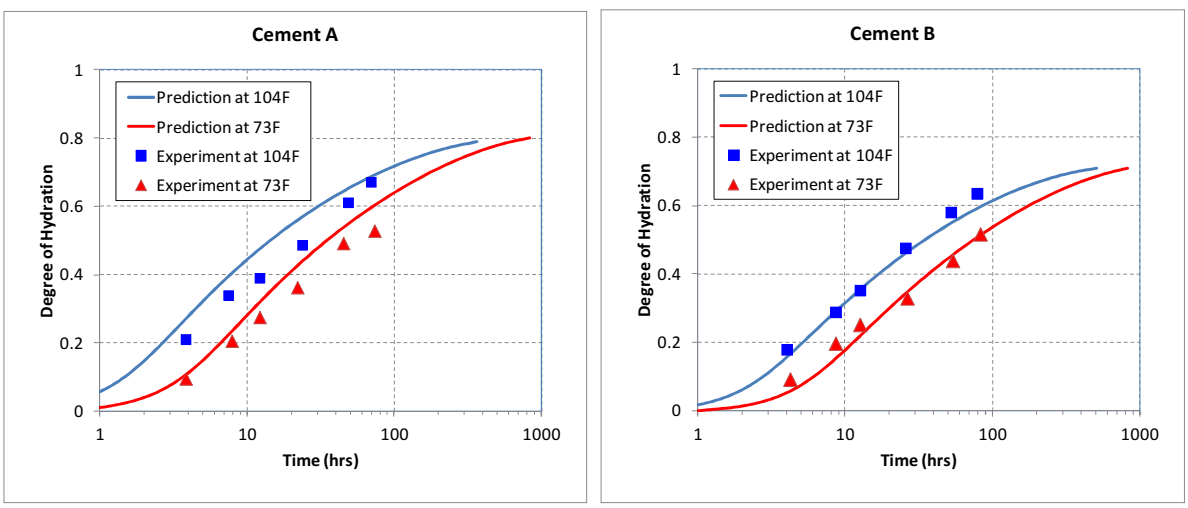

Fig. A.1 Comparison between experimental data and model predictions for cement #A and #B at different temperatures

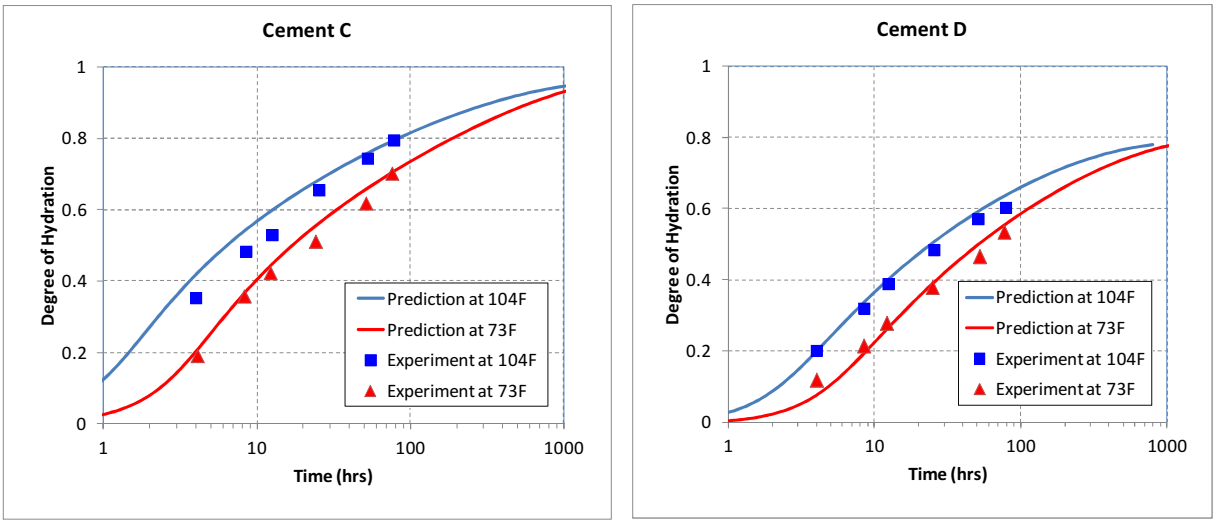

Fig. A.2 Comparison between experimental data and model predictions for cement #C and #D at different temperatures

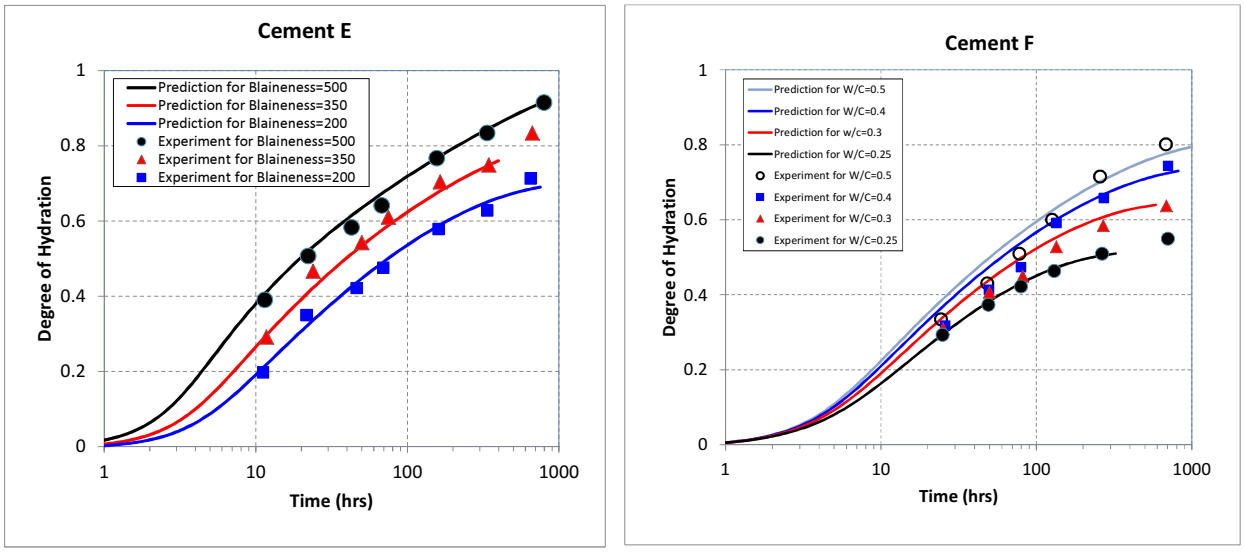

Fig. A.3 Comparison between experimental data and model predictions for cement #E and #F varying cement fineness

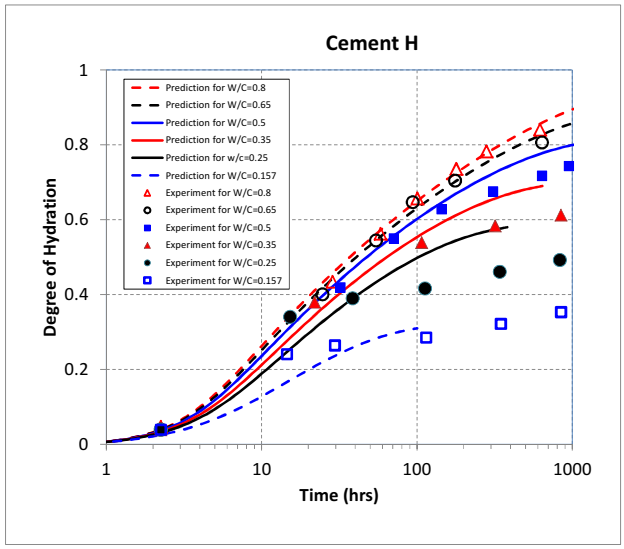

Fig. A.4 Comparison between experimental data and model predictions for cement #H at different water-cement ratios

A.1.5 Model Predictions

A.1.5.1 Initial Porosity

Using the hydration model (Lin and Meyer, 2009), degree of hydration can be obtained as a function of time for different temperatures (Fig. A.5). Degree of hydration can be used to predict the initial porosity of cement, which is important parameter in predicting the leaching rate and consequently mechanical properties and permeability of the cement. Moreover, accurate prediction of the degree of hydration is necessary to determine the appropriate curing time.

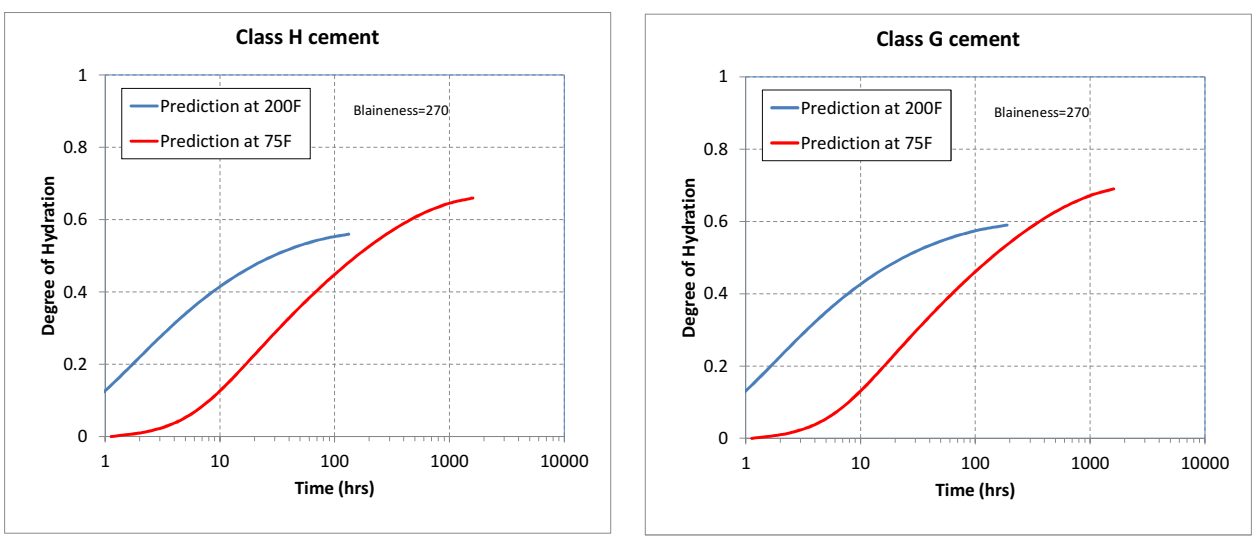

Fig. A.5 Degree of hydration versus time for cement class H and G at different temperatures

Initial porosity of cement after curing is related to the amount of free water present in the cement. The free water available in cement is a function of the degree of hydration, which is affected by cement composition, temperature, water-cement ratio, pressure, and cement fineness. For class H cement, the maximum hydration at temperature of 200°F is about 60% which occurs after 100 hrs (Fig. A.5). Therefore, the amount of water needed for hydration reaction is computed assuming 60 percent cement hydration (Eqs. A.1 through A.5). The procedure for calculating the initial cement porosity is presented here. Three main assumptions of the procedure are:

i. 60% hydration
ii. No volume change while mixing of water and cement
iii. No air entrapment

First, molecular weights of different components of cement need to be determined. Table A.2 summarizes the molecular weight of different components of class H cement, and amount water needed for hydration reaction of each component based on the hydration reactions. The amount of free (unhydrated) water is then calculated by subtracting the amount of water needed for hydration reaction to total amount of water added to the cement to get the desired water-cement ratio. Therefore, total porosity can be calculated by dividing the volume of free water to the total slurry volume (Eq. A.25).

Table A.2 Molecular weight and hydration water requirement of components of class H cement

Element	Molecular Weight	Moles of element	Grams of Element (g)	Moles of water	Grams of Water (g)	Fraction in cement
C_3S	228	2	456	6	108	0.5
C_2S	172	2	344	4	72	0.3
C_4AF	516	1	516	10	180	0.12
C_3A	270	2	540	22	396	0.03

$$Porosity = \phi = \frac{Pore\ Volume}{Bulk\ Volume} = \frac{Extra\ water}{Total\ Slurry\ volume} \quad \text{(A.25)}$$

The porosity of class H cement predicted using this technique is approximately 26%, which shows a good agreement with experimental data obtained using different measuring techniques discussed earlier in Section 2.2. The same procedure is applied for class G cement and porosity of 31.17% is obtained. They main difference between class G and H that causes the variation is the difference in water-cement ratio.

A.1.5.2 Maximum Calcium Concentration

The hydration model not only predicts the amount of free water in the cement but also it provides the concentrations of CH and CSH and subsequently the calcium concentration, which is necessary to predict the leaching rate, mechanical properties and permeability of the cement. In order to determine the calcium concentration in the cement, first CH and CSH produced and consumed by the hydration reactions (i.e. Eqs. A.20 through A.24) have to be calculated. Tables 3 presents predicted CH and CSH concentrations for class H cement. The calcium concentrations in two different cements (H and G classes) obtained from the hydration model is shown in Table 4..

Table A.3 CH and CSH concentrations after hydration for Class H cement

Element	Grams of Element	Moles of element	Moles of CH	Moles of CSH
C_3S	1315.79	5.77	8.66	2.89
C_2S	789.47	4.59	2.29	2.29
C_4AF	315.79	0.61	-1.22	0.00
C_3A	78.95	0.29	-0.29	0.00
Total			**9.44**	**5.18**

Table A.4 Calcium concentrations in CH and CSH phases of Classes H and G cements

	Calcium Concentration (mmol/l)	
	Class H	Class G
CH	9435.1	8148.5
CSH	15541.45	13422.17
Total	24975.55	21570.67

A.1.5.3 Effects of cement additives on maximum calcium concentration

Class G and H cements are intended for use as basic cement from surface to 8000 ft depth as manufactured, or can be used with accelerators and retarders to cover a wide range of well depths and temperatures. Class G and H can be modified easily through the use of additives to meet almost any job specifications economically. The use of modified class H cement has become extremely popular. The cement additives available can be subdivided into these functional groups: i) density control additives; ii) setting time control additives: iii) lost circulation additives; iv) filteration control additives; v) viscosity control additives; and vi) special additives for unusual problems.

Silica fume, which is 100 times smaller than average cement particles, is a very effective pozzolanic material that improves compressive strength, bond strength and permeability of cement. Following is the pozzolanic reaction between silica fume and calcium hydroxide.

$$3[Ca(OH)_2] + 2[SiO_2] = [3(CaO).2(SiO_2).3(H_2O)] \quad (A.26)$$

Adding silica fume (silica) to the cement affects the reaction. Silica reacts with CH and produces CSH. Therefore, adding silica to the cement affects the amount of CH and CSH and consequently changes the calcium content of the cement. As reported by a number of studies (Kosmatka, 2002; Popovics, 1998; Massazza, 1988) only limited portion (20-30%) of free calcium hydroxide reacts with silica. CH and CSH content of the cement and calcium concentration in these two phases change with the addition of silica. Therefore, Reaction equation A.6 should be added to Eqns. A.1 through A.5 to calculate the effect of silica on the amount of CH and CSH. Results presented in Tables 4 and 5 show that adding silica fume to cement decreases the amount of CH while increasing the amount of CSH.

Table A.5 Calcium concentrations in CH and CSH phases of class G cement with silica fume

	Calcium Concentration (mmol/l)
CH	6111
CSH	16477
Total	22588

Appendix B

Literature Review, Theoretical Studies on Tubular Corrosion

Summary

Literature review was conducted on fundamental aspects of CO_2 and H_2S corrosions. Electrochemistry of CO_2 and H_2S corrosion were reviewed from different literature. Comprehensive knowledge of CO_2 and H_2S corrosion electrochemistry will be helpful for corrosion modeling. Different experimental measurement techniques for CO_2 and H_2S corrosions were reviewed. The results of theoretical studies will be used for the experimental part of this project.

The effects of different parameters on CO_2 and H_2S corrosions were reviewed to better understand corrosion process and mechanisms, and develop improved models. The review will continue in the future. Fourteen CO_2 and H_2S corrosion models were reviewed from the available literature. So far, extensive research has been done by different investigators to better understand the CO_2 and H_2S corrosion mechanisms. However, many studies have emphasized on the need for improved CO_2 and H_2S corrosion models, especially for high-pressure high-temperature (HPHT) conditions. In this report, one of the mechanistic models for CO_2 corrosion has studied in details and a modified CO_2 corrosion model has been proposed for non-scale forming conditions. The proposed model will be validated with experimental data in the future. The new model can be extended for scale forming and HPHT conditions. Synergistic effect between CO_2 and H_2S corrosion will be studied on theoretical part of this research and the CO_2 and H_2S models will be coupled.

B.1 Introduction

Corrosion is known as materials degradation as a result of chemical and electrochemical reactions. Corrosion can be divided into several categories based on the mechanism of corrosion reaction including general corrosion, pitting corrosion, crevice corrosion, erosion-corrosion, galvanic corrosion, microbial corrosion, stress corrosion cracking, intergranular corrosion and other uncommon types of corrosion mechanisms. Corrosion environment can be also a good criterion for dividing into different categories based such as CO_2 corrosion, H_2S corrosion, atmospheric corrosion, acid corrosion and high temperature corrosion. In the oil and gas industry, CO_2 and H_2S corrosions are two common types of corrosion, which cause a number of problems during oil and gas production. CO_2 and H_2S are the two well known corrosive gases that are produced. Because of the diversity of corrosion related problems, CO_2 corrosion (sweet corrosion) is probably the material degradation mechanism most extensively

assessed in this industry over the last 30 years. CO_2 is also sometimes injected into oil and gas wells for production enhancement or sequestration purposes. The fundamentals of CO_2 and H_2S corrosion processes, corrosion measurement techniques, effects of different parameters on CO_2 and H_2S corrosion, and a summary of some famous CO_2 corrosion models are presented in the following sections. A modified CO_2 corrosion model for non-scale forming conditions is proposed at the end. Research is in progress on the CO_2 corrosion model to validate the model and extent the model for non-scale forming conditions.

B.2 Fundamental Concepts in CO_2 and H_2S Corrosions

The presence of CO_2 and H_2S in the gas phase enhances the internal corrosion by formation water which may occur in oil well casings and tubings. Internal corrosion control is considered as a major cost item. It is estimated (Heidersbach, 2011) that the total annual cost of corrosion in the U.S. oil and gas production industry is roughly $1.372 billion/year The annual corrosion cost for oil and gas production was estimated to be approximately eight percent of the total production and manufacturing category cost (Fig. B.1).

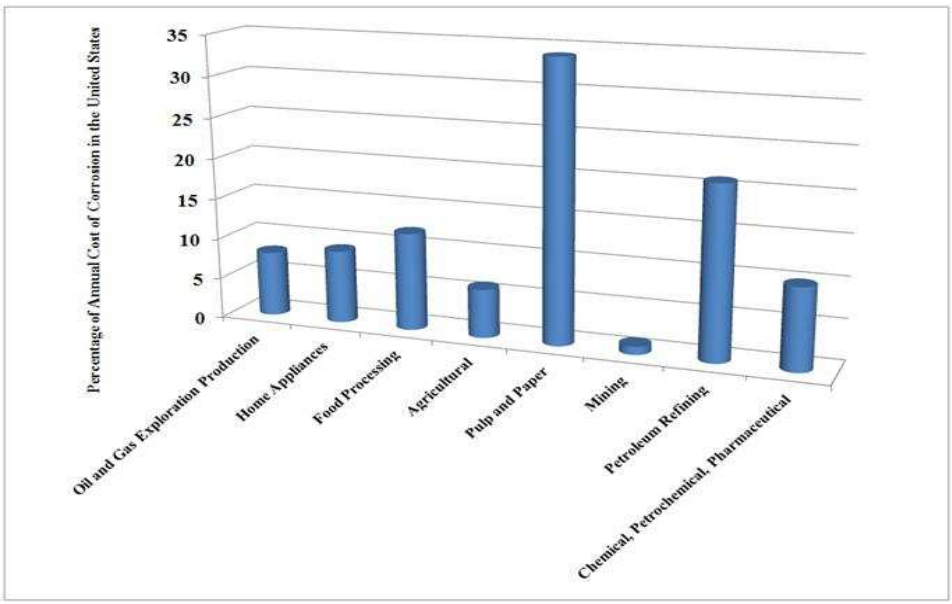

Fig. B.1 Annual cost of corrosion of oil and gas exploration industry (Heidersbach, 2011)

B.2.1 Electrochemistry of CO_2 Corrosion

The overall reaction for aqueous CO2 corrosion of carbon steel is:

$$Fe + CO_2 + H_2O \rightarrow FeCO_3 + H_2 \quad \text{(B.1)}$$

CO_2 corrosion of carbon steel involves anodic dissolution of iron and cathodic evolution of hydrogen. The anodic dissolution for iron in acid solutions (shown below) has been studied extensively with several multi-step mechanisms suggested to explain the various experimental results.

$$Fe \rightarrow Fe^{++} + 2e^{-} \quad \text{(B.2)}$$

The reaction is pH dependent in acidic solutions with a reaction order with respect to OH^- between 1 and 2, decreasing toward 1 and 0 at pH > 4 (Nesic, 2007). It has been reported (Nesic, 2007) that the anodic dissolution of iron is affected by the presence of CO_2. The carbonic species acts as a chemical ligand and catalyses the dissolution creating different kinetics of iron dissolution in CO_2 solutions compared to strong acids. It is assumed the ligand $Fe_L = Fe–CO_2$ is formed as an adsorbed species at the electrode surface. H_2CO_3 and dissolved CO_2 are the only carbonic species whose concentrations do not depend on pH. Therefore, formation of this ligand is independent of pH. Several detailed multi-step models have been presented to explain the various findings. The following corrosion mechanism has been developed by Nesic et al. (1996) to explain the experimental results for pH > 5.

$$\mathrm{Fe + CO_2 \Leftrightarrow Fe_L} \quad \text{(B.3a)}$$

$$\mathrm{Fe_L + H_2O \Leftrightarrow Fe_LOH_{ad} + H^+ + e^-} \quad \text{(B.3b)}$$

$$\mathrm{Fe_LOH_{ad} \xrightarrow{rds} Fe_LOH_{ad}^+ + e^-} \quad \text{(B.3c)}$$

$$\mathrm{Fe_LOH_{ad}^+ + H_2O \Leftrightarrow Fe_L(OH)_{2ad} + H^+} \quad \text{(B.3d)}$$

$$\mathrm{Fe_L(OH)_{2ad} \Leftrightarrow Fe_L(OH)_{2sol}} \quad \text{(B.3e)}$$

$$\mathrm{Fe_L(OH)_{2sol} + 2H^+ \Leftrightarrow Fe^{2+} + CO_2 + 2H_2O} \quad \text{(B.3f)}$$

The presence of CO_2 increases the rate of corrosion of iron in aqueous solutions by increasing the rate of the hydrogen evolution reaction. In strong acids, which are completely dissociated, the rate of hydrogen evolution cannot exceed the rate of mass transfer at which H^+ ions can be transported to the surface from the bulk solution. In solutions with a pH > 4, the mass-transfer-controlled limiting current is small and the presence of H_2CO_3 enables hydrogen evolution at a much higher rate. Thus, at a given pH, the presence of CO_2 leads to a much

higher corrosion rate than would be found in a solution of a strong acid. Despite more than three decades of intense research, it is still not known with absolute certainty whether H_2CO_3 is reduced directly (as assumed by many workers in the field) or the final step in the reaction follows the dissociation of the H_2CO_3. Many researchers (Nesic, 2007, Gray et al., 1989; Bonis and Crolet, 1989) have assumed that the two reactions are independent and the net cathodic current is the sum of the currents for the two reactions.

$$2H^+ + 2e^- \rightarrow H_2 \quad \text{(B.4)}$$

$$2\,H_2CO_3 + 2e^- \rightarrow H_2 + 2HCO_3 \quad \text{(B.5)}$$

At pH > 5 and very low partial pressures of CO_2, hydrogen evolution from the direct reduction of water which occurs at lower potentials becomes important (Schmitt and Rothmann, 1977, Nesic et al. 1995).

$$2H_2O + 2e^- \rightarrow H_2 + 2OH^- \quad \text{(B.6)}$$

Gray et al. (1989) have suggested that at higher pH in CO_2 solutions, the direct reduction of the bicarbonate ion becomes important:

$$2HCO_3^- + 2e^- \rightarrow H_2 + 2CO_3^{2-} \quad \text{(B.7)}$$

Because of increasing concentrations of bicarbonate at higher pH, it is difficult to distinguish the reaction path for hydrogen evolution experimentally. It has been observed that in the range of 4 < pH < 7, the corrosion rates steadily decrease with increasing pH bringing the significance of reaction shown in Eq. (B.7) in the overall reaction while the concentration of bicarbonate ion steadily increases.

B.2.2 Electrochemistry of H_2S Corrosion

Fast and direct heterogeneous chemical corrosion reaction of H_2S with carbon steel causes the formation of mackinawite corrosion product scale on the metal surface. The overall reaction can be written as:

$$FeS(S) + H_2S \rightarrow FeS(s) + H_2 \quad \text{(B.8)}$$

This reaction can be referred as a “solid state corrosion reaction” since both the initial and final state of Fe is solid. The mackinawite formed during corrosion reaction may dissolve depending on the level of solution saturation. Oilfield brines have the typical pH range of 4 to 7, which is

usually supersaturated with respect to iron sulfide. Therefore, mackinawite scale layer does not dissolve (Brown et al., 2004). The mackinawite formed during corrosion reaction starts dissolving for pH below 4. Mackinawite dissolution increases with decreasing the pH up to the pH of 2 to 3 which all the mackinawite will dissolve in brine (Shoesmith et al. 1980).

B.3 CO_2 and H_2S Corrosion Measurement Techniques

Corrosion measurement techniques can be divided to two main categories known as non-electrochemical and electrochemical. Non-electrochemical techniques are including weight loss measurement, 3D profilometer of surface, visual observations, electrical resistance probes and ultrasonic measurement techniques. The electrochemical measurement techniques are including Linear Polarization Resistance (LPR), Electrochemical Impedance Spectroscopy (EIS), Potentiodynamic polarization, Electrochemical Frequency Modulation (EFM), Harmonics and electrochemical noise. A summary of two important electrochemical measurement techniques used in this study are discussed in the following sections. More details about electrochemical measurement techniques can be found in ASTM G3, Standard Practice for Conventions Applicable to Electrochemical Measurements in Corrosion Testing.

B.3.1 Linear Polarization Resistance

A widely used polarization method is linear polarization resistance (LPR). The polarization resistance of a material is defined as the slope of the potential–current density (*E-i*) curve (i.e. Tafel slope) at the free corrosion potential (Fig. B.2), yielding the polarization resistance *Rp,* which can be itself related to the corrosion current with the help of:

$$R_p = \frac{B}{i_{corr}} = \frac{\Delta E}{(\Delta i)_{\Delta E \to 0}} \quad \text{(B.9)}$$

where:

R_p = Polarization Resistance

i_{corr}= Corrosion Current

B = Empirical polarization resistance constant that can be related to the anodic (b_a) and cathodic (b_c) Tafel slopes with

$$B = \frac{b_a b_c}{2.3(b_a + b_c)} \quad \text{(B.10)}$$

The Tafel slopes themselves can be evaluated experimentally using real polarization plots similar to those presented in Fig. B.3 and B.4 or obtained from literature (Roberge, 1999).

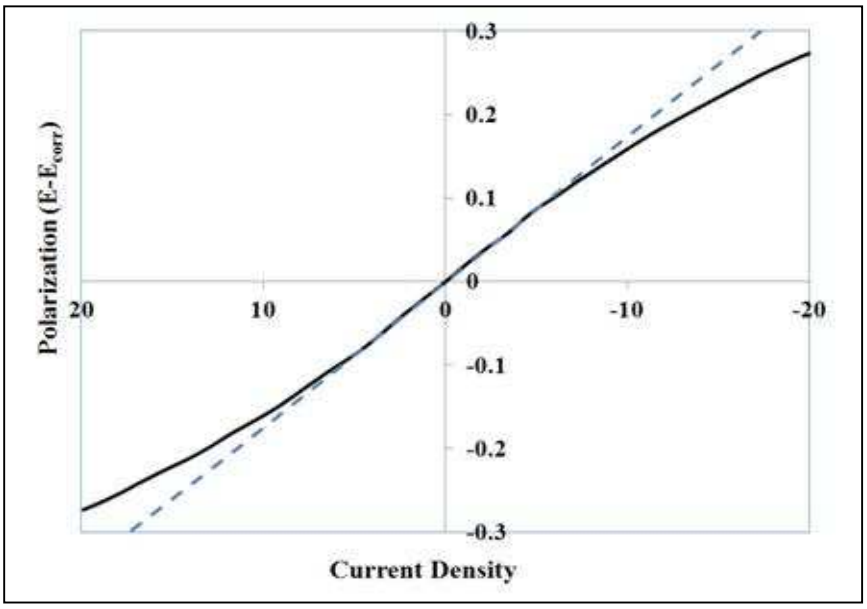

Fig. B.2 Hypothetical linear polarization plot (Roberge, 1999)

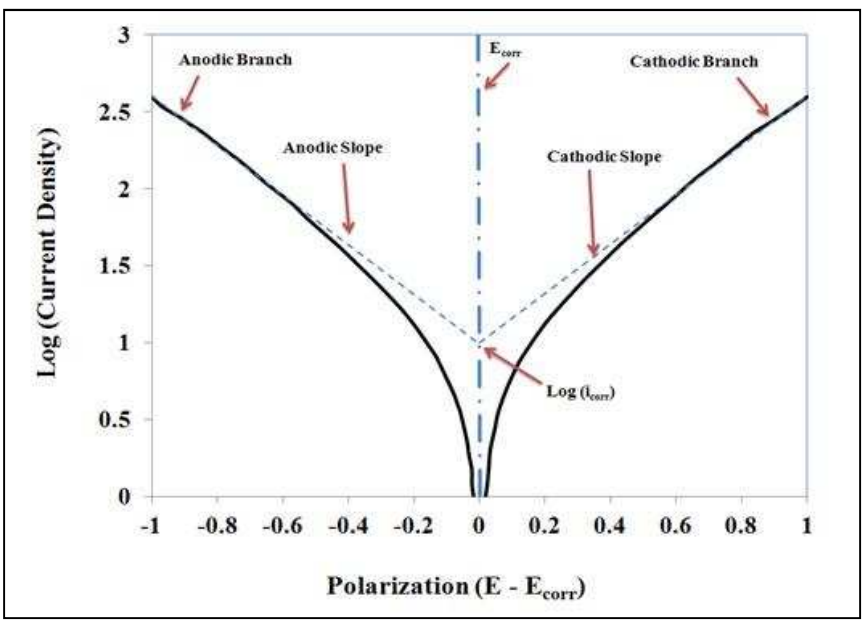

Fig. B.3 Hypothetical polarization diagram for an active system with anodic and cathodic branches (Roberge, 1999)

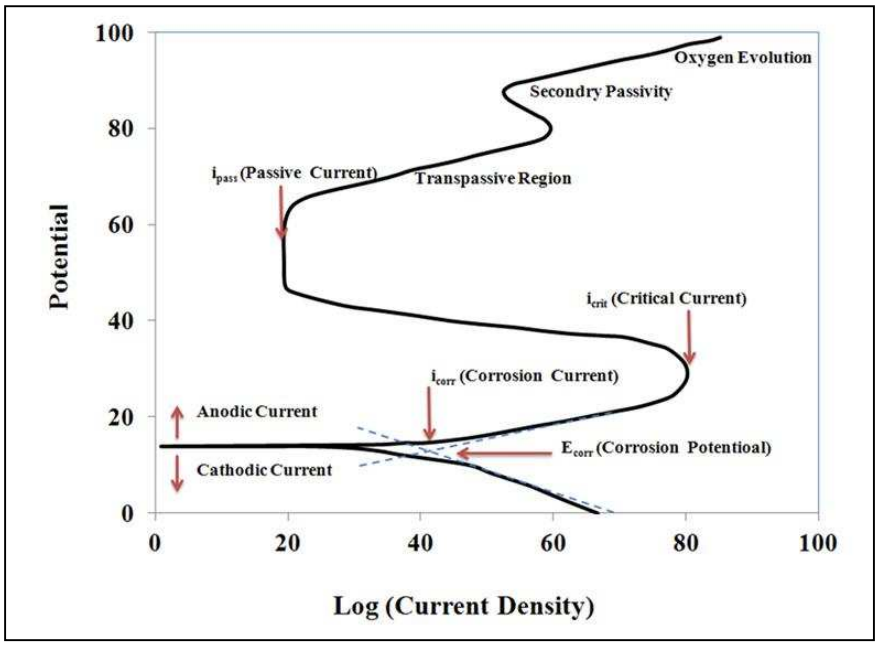

Fig. B.4 Hypothetical polarization diagram for a passivating system with anodic and cathodic branches (Roberge, 1999)

B.3.2 Electrochemical Impedance Spectroscopy

Electrochemical impedance spectroscopy (EIS) has been successfully applied to the study of corrosion systems since early seventieth; and it has been proven to be a powerful and accurate method for measuring corrosion rates. However, to determine the charge transfer resistance or polarization resistance R_p, which is proportional to the corrosion rate at the monitored interface, EIS results have to be interpreted with the help of a model of the interface. Since the early work published by Epelboin and coworkers, EIS has gained tremendous momentum and popularity in corrosion laboratories around the world (Epelboin et al. 1972). The advantage of EIS over other laboratory techniques is the possibility of using very small-amplitude signals without significantly affecting the properties being measured. To make an EIS measurement, a small-amplitude signal, usually a voltage between 5 and 50 mV, is applied to a specimen over a range of frequencies from 0.001 to 100,000 Hz.

The EIS technique monitors the real (resistance) and imaginary (capacitance) parts of the impedance response of the system. An electrical circuit model or circuit description code and initial circuit parameters are assumed depending upon the shape of the EIS spectrum. A computer program can be used to fit the best frequency response to the given EIS spectrum to calculate the EIS spectrum parameters. Depending upon how well the fitting curve overlaps the original spectrum, the quality of the fitting can be judged. It is possible to obtain a set of parameters by fitting the EIS data, which can be correlated with the corrosion of the substrate,

electrochemical reactions, and the coating condition (if a coating is present). Only a few numerous equivalent circuits really apply in the context of a freely corroding interface at or close to kinetic equilibrium to describe electrochemical interfaces. The first circuit (Fig. B.5*a*) corresponds to the simplest equivalent circuit that can describe a metal/electrolyte interface. The component *Q* describes the "leaky capacitor" behavior corresponding to the presence of a constant phase element. The admittance representation Y^* of the CPE behavior with frequency can be described by Eq. (B.10). For $n = (1-\beta)$, Eq. (B.10) describes the behavior of a resistor with $R = Y_o^{-1}$ and for $n = \beta$, that of a capacitor with $C = Y_o$. For $n = 0.5$, Eq. (B.10) becomes the expression of a Warburg (W) component, and when $n=-\beta$, it emulates an inductance with $L = Y_o^{1.25}$ (Epelboin et al. 1972).

$$Y^*(\omega) = Y_o\, \omega^{n} \cos(n\pi/2) + jY_o\, \omega^{n} \sin(n\pi/2) \quad \text{(B.11)}$$

Figure B.6 illustrates the complex-plane presentation of EIS simulated data corresponding to the model circuit in Fig. B.5(a) when R_s =10 Ω, R_p =100 kΩ, and *Q* decomposes into C_{dl} = 40 μF and n = 0.8, and Fig. B.7 shows how the same data would appear in a Bode plot format (Epelboin et al. 1972).

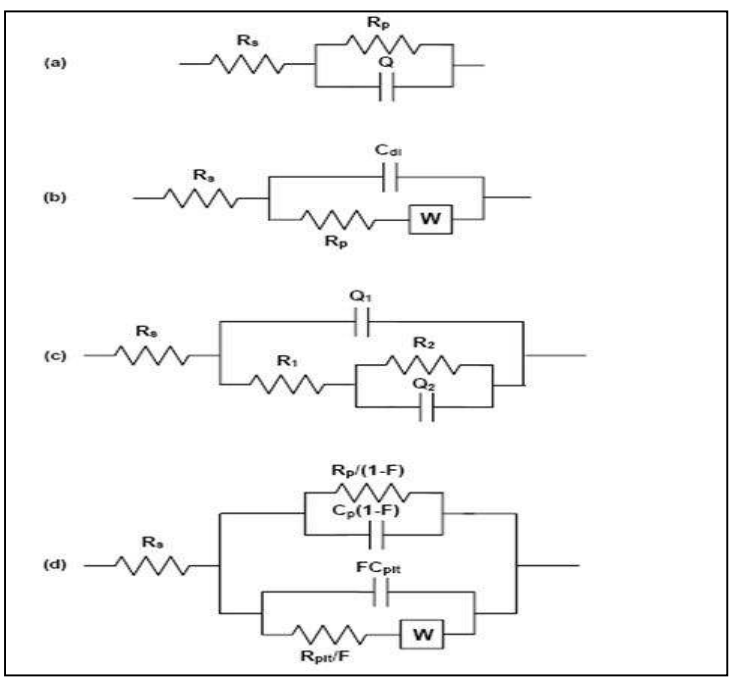

Fig. B.5 Equivalent circuit models proposed for the interpretation of EIS results measured in corroding systems: (a) simplest representation of an electrochemical interface; (b) one relaxation time constant with extended diffusion; (c) two relaxation time constants; and (d) the impedance of pitting processes of Al-based materials (Epelboin et al. 1972)

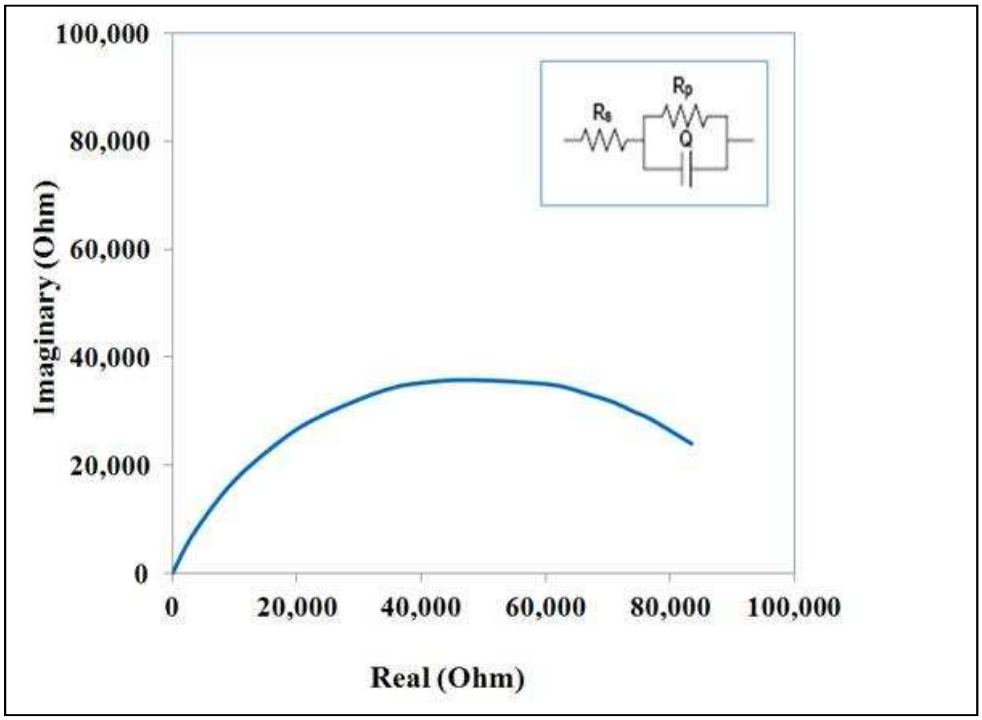

Fig. B.6 Complex-plane presentation of simulated data corresponding to the model circuit in Fig. B.5a when R_s=10 Ω, R_p= 100 KΩ, and Q decomposes into C_{dl}=40μF and n=0.8 (Epelboin et al. 1972)

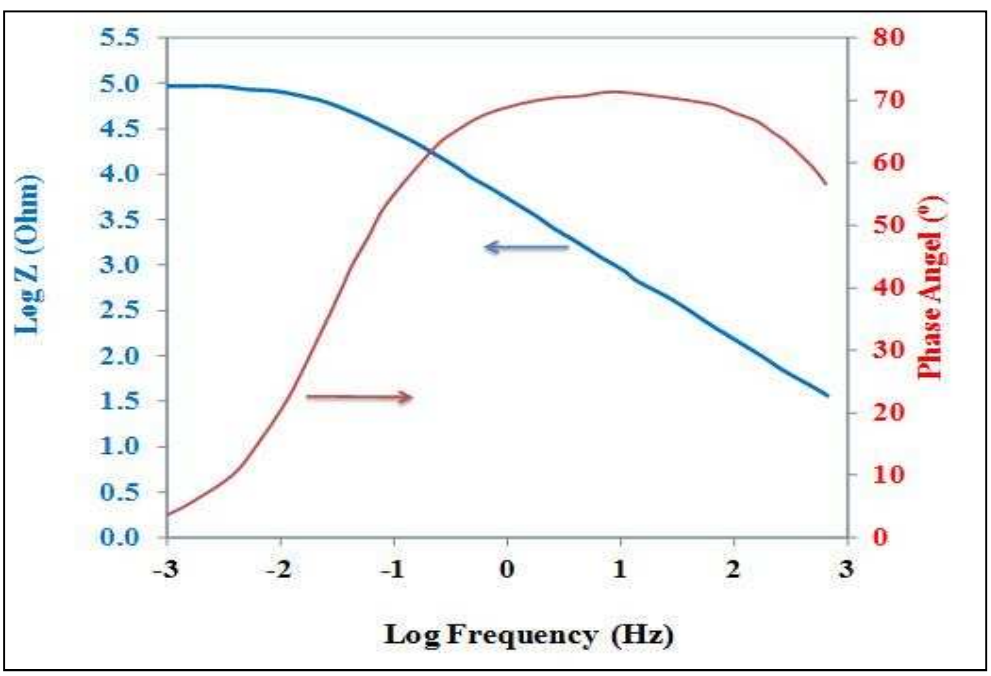

Fig. B.7 Bode representation of the same data illustrated in Fig. B.6 in complex plane format (Epelboin et al. 1972)

B.4 Effects of Different Parameter on CO_2 Corrosion

The most important parameters affecting the CO_2 corrosion behavior are NaCl concentration, pH, temperature, flow velocity, flow regime, and CO_2 pressure. More details about the effect of each parameter on CO_2 corrosion are discussed in the following sections.

B.4.1 Effect of NaCl on CO2 Corrosion

Oil and gas formations usually contain large amounts of brine (altered seawater trapped in sediment pores). Chloride concentration can vary significantly, on average, produced brine during oil and gas production contains 50,000 mg/L chloride (Hudak and Wachal, 2001), which is corrosive to metals.

Previous work by Uhlig et al. (1985) reported decreased oxygen corrosion with increased NaCl concentration in brine solutions. According to their investigation, increasing the amount of chloride in solution increases the conductivity and consequently the corrosion rate until a critical amount of NaCl (3 wt% NaCl) and, after that, increasing the chloride content will decrease the corrosion rate by decreasing the solubility of the corrosive agent (oxygen in their investigation). Hassani et al. (2011) reported a slight reduction in CO_2 corrosion rate of carbon steel by increasing the NaCl concentration from 3 to 18% (by weight). On the other hands, Fang et al. (2010) reported a considerable change in corrosion rate by increasing the NaCl concentration in brine solution. Increasing the NaCl concentration from 1 to10 wt% was reported to reduce the CO_2 corrosion rate by changing the density and viscosity, which affect the mass transfer processes, from an increase in ionic strength, which reduces the amount of dissolved CO_2, and from chloride ion adsorption onto the metal surface. At 20ºC, the corrosion mechanism gradually changes from mixed charge transfer/limiting current control to pure charge transfer control with the increase of salt concentration.

An increase in salt concentration retards the heterogeneous charge transfer reactions, as well as the homogenous chemical reactions and the mass transfer. Previous investigations on the effect of high ionic strength on CO_2 corrosion show that iron carbonate scale formation is a function of the ionic strength of the solution. In general, higher salt concentrations lead to higher values of the solubility limit for precipitation and growth of $FeCO_3$ scale (Silva et al., 2002; Sun et al., 2009). Therefore, under environmental conditions for which iron carbonate precipitation would be expected when NaCl concentration is low, if the NaCl concentration is increased, iron carbonate may no longer precipitate. Fosbøl et al. (2009) discussed the effect of high ionic strength on the diffusion process during CO_2 corrosion and the importance of including this effect in mechanistic models for CO_2 corrosion prediction.

B.4.2 Effect of pH on CO_2 Corrosion

The pH of a solution has substantial effect on CO_2 corrosion behavior. Formation of iron carbonate scale at high pH decreases the CO_2 corrosion considerably. At pH 4 or below, direct reduction of H^+ ions is important particularly at lower partial pressure of CO_2 and the pH has a direct effect on the corrosion rate. However, the most important effect of pH is indirect and relates to how pH changes conditions for formation of iron carbonate scales. High pH results in a decreased solubility of iron carbonate and leads to an increased precipitation rate and higher scaling tendency. Experimental results by Chokshi et al. (2005) indicated that at lower super-saturations obtained at pH = 6.0, the corrosion rate does not change much with time, even if some iron carbonate precipitation occurs, reflecting the fact that a relatively porous, detached and non-protective scale is formed. Higher pH (pH = 6.6) results at higher super-saturation indicated faster precipitation and formation of more protective scales, reflected by a rapid decrease in the corrosion rate with time.

pH also has some indirect effects, for example: increasing the ratio of Ac^-/HAc with pH makes the acetic acid less corrosive; high pH causes the formation of different types of corrosion products. Lower corrosion rate is usually expected at higher pH which makes the "pH stabilization" (meaning pH increase) technique an attractive way of managing CO_2 corrosion. On the other hand, it can lead to excessive scaling and can be rarely used to control corrosion caused by formation water systems (Nesic, 2007).

B.4.3 Effect of Temperature on CO_2 Corrosion

Temperature affects corrosion behavior by accelerating all the phenomena involved, including electrochemical, chemical, and transport processes. Increasing the temperature may increase or decrease the CO_2 corrosion rate depending upon the precipitation of iron carbonate scale. The corrosion rate (measured using the weight loss technique) steadily increases with temperature at low pH for which precipitation of iron carbonate or other protective type of scale does not form (Fig. B.8). The situation changes markedly when solubility of iron carbonate (or another salt) is exceeded, typically at a higher pH. In that case, increased temperature rapidly accelerates the kinetics of precipitation and protective scale formation, decreasing the corrosion rate. The peak in the corrosion rate is usually seen between 60℃ and 80℃ depending on water chemistry and flow conditions.

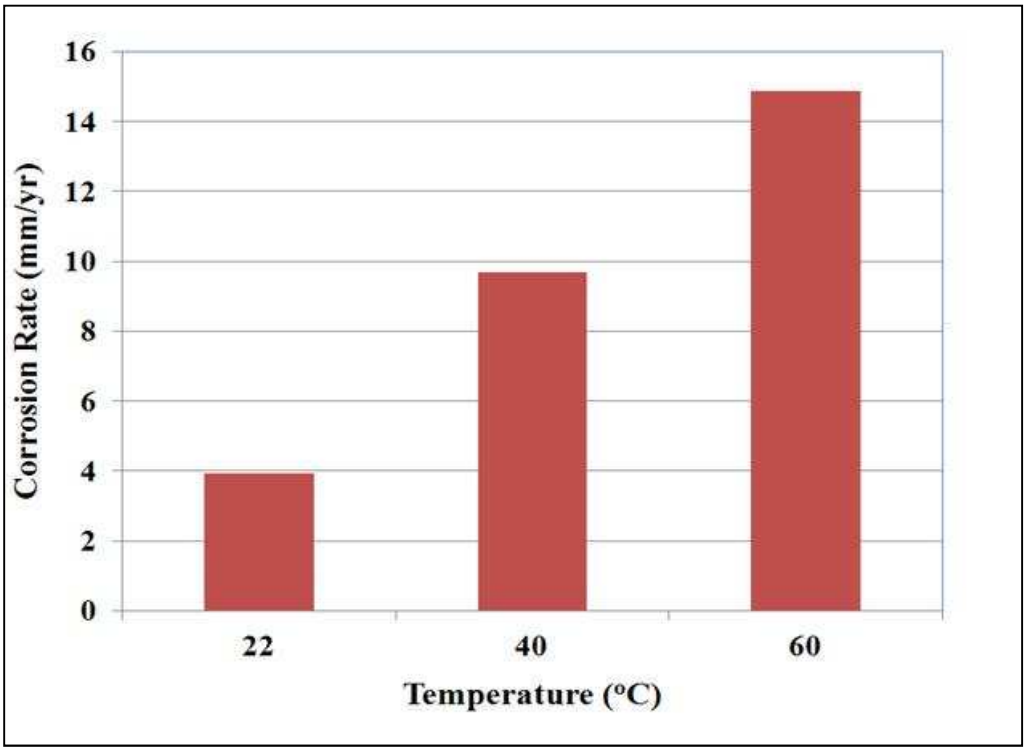

Fig. B.8 Corrosion rates vs. temperature, pH 4, P_{CO2}=1 bar, C_{Fe2+} < 5ppm, 100 ppm acetic species (HAc + Ac^-), v = 0.5 m/s (Nesic, 2007)

B.4.4 Effect of Flow Velocity and Flow Regime on CO_2 Corrosion

There are two main ways in which flow may affect CO_2 corrosion which can be distinguished based on whether or not other conditions are conducive to protective scale formation. Turbulent flow condition favors the transport of species towards and away from the metal surface when no protective scales form during corrosion which usually happens at low pH. In this case, higher corrosion rate would be expected as illustrated in Fig. B.9. The figure compares model (Nesic et al., 1995) predictions with published experimental results (Nesic, 2004).

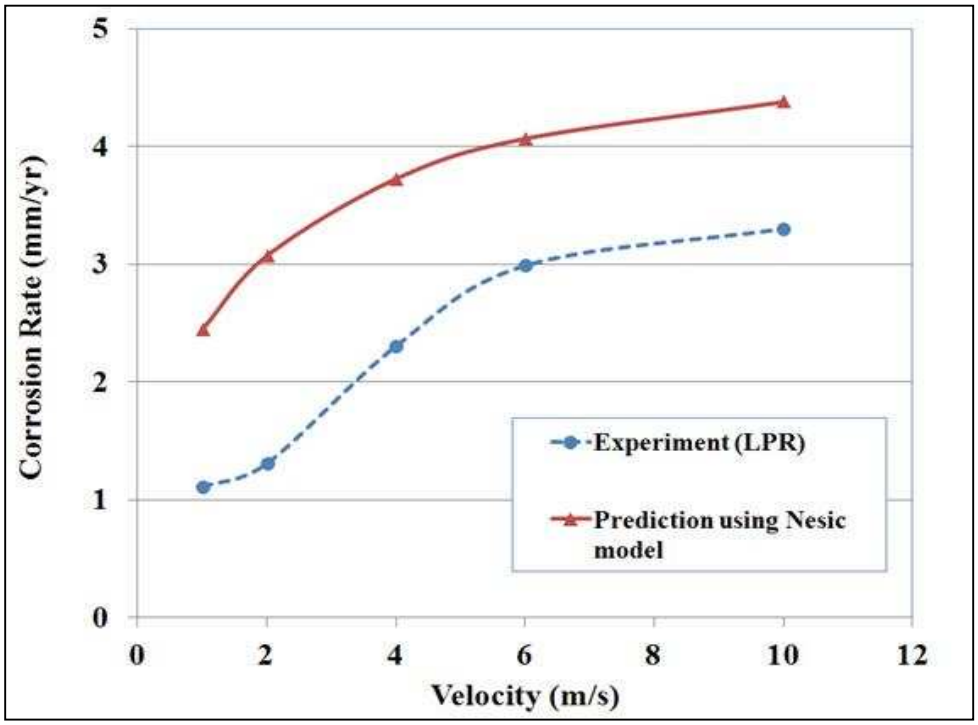

Fig. B.9 Predicted and measured corrosion rates showing the effect of fluid velocity in the absence of iron carbonate scales at 20℃, P_{CO2}=1 bar, C_{Fe}^{2+} <2 ppm.

Modification of flow distribution system such as constrictions, bends, elbows, plugged tees, valves, expansions, extractions, etc. is a usual approach for reducing the flow accelerated corrosion effects discussed earlier. Unsteady slug flow can also lead to considerable fluctuations in wall shear stress and removes the protective surface scale layer or remove the protective inhibitor films from carbon steel substrate.

Zhang and Cheng (2009) studied the effects of flow velocity and impact angle on CO_2 corrosion for direct impingement geometry using computational fluid dynamics and corrosion experiments in CO_2 saturated systems. The role of fluid hydrodynamics in the CO_2-containing solution depends on its effect on the iron-carbonate scale formation. An increasing flow velocity and shear stress could thin, degrade, or even remove completely the scale, thus increasing corrosion rate of the steel. During fluid impingement, the shearing effect in the lateral direction increases with the decreasing impact angle, accelerating the removal of the corrosion scale from the steel surface. Therefore, an oblique impact of fluid would generally result in a high corrosion rate of the steel.

The effect of impact angle on corrosion of the steel is attributed to the distribution of fluid flow field and shear stress on the electrode surface. A low flow velocity and shear stress and thus a low mass transfer rate would be generated at the centric regions at the normal impact. Therefore, a compact corrosion scale can be formed on the electrode surface to protect the steel. The high flow velocity and shear stress adjacent to the center causes higher corrosion

rate in the region. The corrosion rate decreases with the increase in radial distance due to high flow velocity and shear stress. The fluid flow velocity and shear stress, and consequently the corrosion rates are higher at the side of the impingement pattern at the oblique impact angles. The corrosion activity of a steel electrode located at the center of the sample holder generally increases with the decreasing impact angle due to the enhancing effect of shear on the corrosion scale (Zhang and Cheng, 2009).

B.4.5 Effect of CO_2 Pressure on CO_2 Corrosion

The impacts of temperature and CO_2 partial pressure on the rate of corrosion of carbon steel are shown in Fig. B.10 as presented by Ropital (2010).

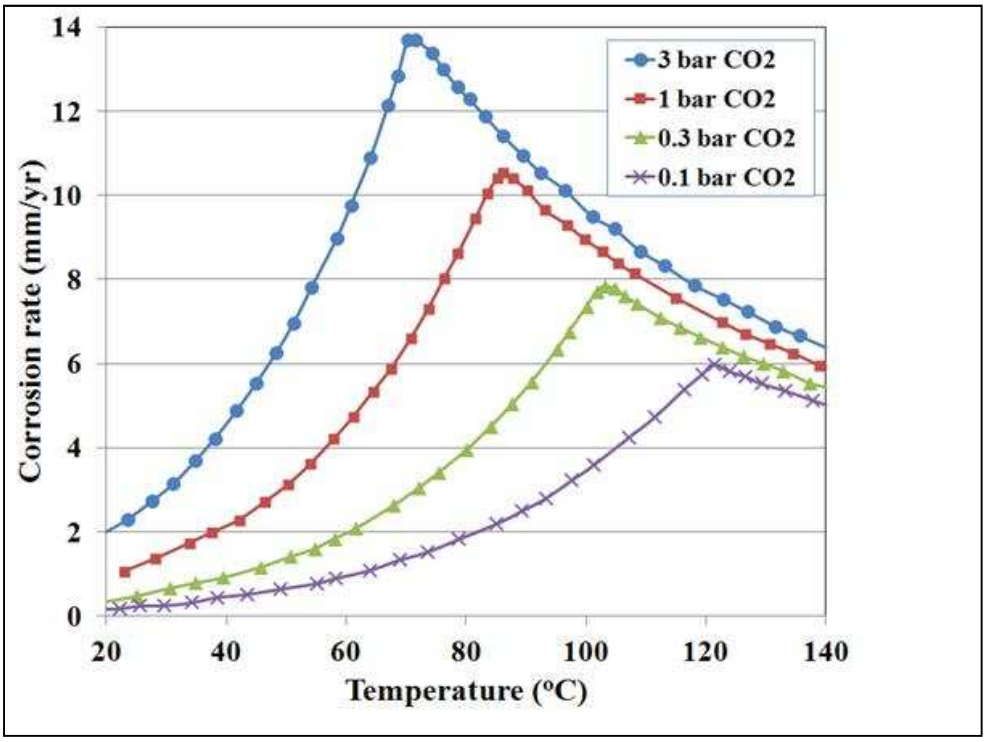

Fig. B.10 Influence of temperature and CO_2 partial pressure on the rate of corrosion of carbon steel (Ropital, 2010)

In the case of scale-free CO_2 corrosion, increase in CO_2 partial pressure (P_{CO_2}) typically leads to increased corrosion rate. The commonly accepted explanation for this observation is that with P_{CO_2} the concentration of H_2CO_3 increases and accelerates the cathodic reaction and ultimately the corrosion rate. The effect of P_{CO_2} is illustrated in Fig. B.11. The figure compares experimental data (Wang et al., 2004) with model prediction (SPPS:CO_2 1998). However, when other conditions are favorable for formation of iron carbonate scales, increased P_{CO_2} can have a beneficial effect in hindering the corrosion process. At a high pH, higher P_{CO_2} leads to an

increase in bicarbonate and carbonate ion concentration and a higher super saturation, which accelerates precipitation and scale formation.

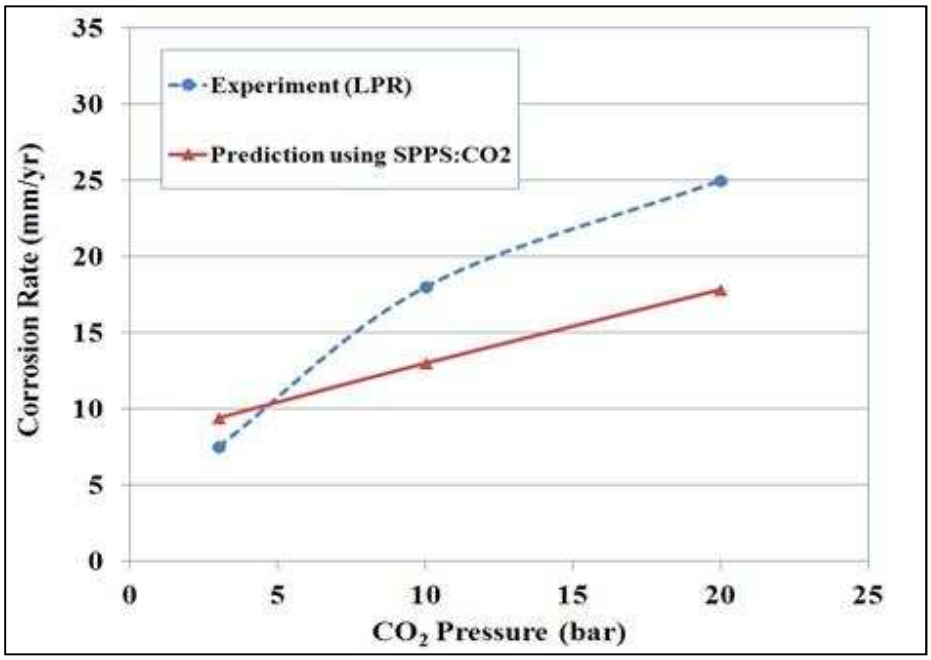

Fig. B.11 Predicted and measured corrosion rates showing the effect of CO_2 partial pressure at 60℃, pH 5, 1 m/s

B.5 Summary of Available CO_2 and H_2S Corrosion Models

There are numerous CO_2 and H_2S corrosion models available in the literature for prediction of corrosion rate and also for predicting the thickness and protective properties of corrosion products. Nyborg (2010) summarized the characteristics of fourteen CO_2/H_2S corrosion models used in the oil and gas industry and discussed the abilities and limitations of these models. Next paragraphs are the summary of these fourteen models, which were presented by Nyborg (2010). Most of these models are for pure CO_2 corrosion.

B.5.1 De Waard Model

de Waard and coworkers (hereafter denoted Model DW) developed a corrosion model which was used for several years (de Waard and Milliams, 1975: de Waard et al., 1991: de Waard et al., 1995). The effect of protective corrosion scale was not completely considered in this model.

B.5.2 Norsok M-506 Model

Norsok M-506 which hereafter denoted Model NO is an empirical model (Norsok, 1998; Halvorsen and Søntvedt, 1999). The same experimental data as DW model was used to calibrate this model plus some more experimental data at higher temperature to have a better prediction for scale forming conditions. This model is also more sensitive to pH in comparison with DW.

B.5.3 Hydrocor

Hydrocorr, which hereafter will be denoted as Model HY, is a combine corrosion and fluid flow modeling developed by Shell (Pots, 1995: Pots et al., 2002: Pots and Kapusta, 2005). A simplified H_2S corrosion model is also included in this model. The scale factor used in this model predicts a relatively low protection. This model works for multiphase flow conditions as well.

B.5.4 Corplus

Corplus is another CO_2 corrosion model which is developed by Total. This model will be denoted as Model CO hereafter (Bonis and Crolet, 1989; Crolet and Bonis, 1991; Gunaltun, 1996). This model is calibrated based on corrosion data obtained from oil and gas wells. Detailed analysis of the water chemistry is the base of this model.

B.5.5 Cassandra

Cassandra which is developed by BP will be denoted as Model CA hereafter (Hedges et al., 2005). In this model, user has the option to include or exclude the effect of protective scale layer. pH of the solution is also calculated as a function of CO_2 content, temperature, and full water chemistry.

B.5.6 KSC Model

KSC is also another CO_2 corrosion model, which will be denoted as Model KS hereafter (Nordsveen et al., 2003; Nesic et al., 2003). This model was developed by coupling the electrochemical model (Nesic et al., 1996) with species transport model. The model predicts different steps of corrosion reaction including electrochemical reactions at the steel surface, chemical reactions in the liquid phase, diffusion of species to and from the bulk phase, and diffusion through porous iron carbonate films. Effect of protective scale layer is appropriately included in this model. The model is able to predict low corrosion rates at high pH and temperature.

B.5.7 Multicorp

Ohio University also developed a CO_2 corrosion model, which will be denoted as Model MU hereafter. The basic idea of this model comes from KS model (Nordsveen et al., 2003). Multiphase flow was included in this model to extend the capabilities of this model. Effect of oil wetting and chemistry of crude oil were also included in this model. This model was verified against the experimental and field data. Effect of H_2S on CO_2 corrosion is also included in this model. Iron sulfide scale formation and iron carbonate scale formation and growth are modeled. This model is also able to handle the localized attack.

B.5.8 ECE Model

ECE is a CO_2 corrosion model developed based on DW model, which hereafter will be denoted as Model EC (de Waard et al., 2003; Smith and de Waard, 2005). This model is developed for wells and flow lines. It is able to predict the effect of small amount of H_2S. Small amount of H_2S can lead to considerable drop in corrosion rate because of formation of protective scale layer of iron sulfide. Model predictions are not very sensitive to pH.

B.5.9 Predict

Predictive model, which was developed by Honeywell, will be denoted as Model PR hereafter (Srinivasan and Kane, 1996; Sangita and Srinivasan, 2000; Srinivasan and Kane, 2003). This model is also based on DW model. Flow velocity and flow regime are incorporated in this model. Model predictions are sensitive to change in pH of solution.

B.5.10 Tulsa Model

University of Tulsa developed a CO_2 corrosion model which is called SSPS CO_2 corrosion model and hereafter will be denoted as Model TU (Dayalan et al. 1995; Dayalan et al. 1998; Adsani et al., 2006). The model is able predict the CO_2 corrosion rate in single phase and two phase flow condition. In addition, it predicts the formation of iron carbonate scale. The model considers a number phenomena that affect corrosion including chemical reaction in bulk solution, electrochemical reaction on the metal surface, mass transfer from the bulk to the metal surface, and also mass transfer from the metal surface to the bulk solution. More details of this model are provided in section B.6.

B.5.11 ULL Model

ULL which is developed at the University of Louisiana at Lafayette will be denoted as Model UL hereafter (Perkins et al., 1996; Garber et al., 1998). This model is able to predict the flow regime and the location for condensation of water and hydrocarbons in well. It is also able to predict the temperature, pressure, pH and corrosion rate profiles along the well.

B.5.12 CorPos

CorPos will be denoted as Model CP hereafter. This model is a combination of multiphase flow model, water chemistry model, and corrosion model, which is able to predict the CO_2 corrosion rate and pH of the solution along the pipe (Gartland and Salomonsen, 1999; Gartland et al., 2003). Bicarbonate produced by the corrosion reaction is also included for pH calculation. The model predicts the corrosion rate in several points along the pipe.

B.5.13 OLI Model

OLI CO_2 corrosion prediction model is denoted as Model OL hereafter. This model is a combination of thermodynamic, chemical and electrochemical reaction models. The model predicts the effect of H_2S on formation and dissociation of protective scale layers (Anderko and Young, 1999; Anderko, 2000). Parameters used in this model for scale formation has been calibrated against laboratory data.

B.5.14 SweetCor

SweetCor CO_2 corrosion model, which is developed by Shell. It is based on a large database of corrosion rate data (John et al., 1998). The model uses empirical correlations to predict corrosion rate for specific conditions.

Table B.1 by Nyborg 2010, summarizes the characteristics of these fourteen CO_2/H_2S corrosion models.

Table B.1. Important factors in CO_2/H_2S corrosion prediction models (Nyborg, 2010)

Model	DW	NO	HY	CO	CA	KS	MU	EC	PR	TU	UL	CP	OL	SW
Lab data, **F**ield data model, **M**echanistic model	L	L	M	F	L	M	M	L	L	M	F	L	M	L
Scale effect formation water*	N	M	N	W	W	M	M	W	S	S		M	W	W
Scale effect condensed water*	W	M	W	W	W	M	M	W	S	S		M	M	W
Effect of pH on corrosion rate*	W	M	W	M	W	M	M	W	S	S	S	M	W	W
Risk for localized attack				Y		Y			Y		Y			
Oil wetting effect crude oil*	S	N	M	M	N	N	S	S	S	N	S	M	N	N
Oil wetting effect condensate*	N	N	N	M	N	N	M	M	M	N	S	M	N	N
$CaCO_3$ correction for pH				Y			Y						Y	
Effect of organic acid on corrosion			Y	Y	Y		Y	Y	Y		Y			
Top of line corrosion	Y		Y				Y	Y			Y			
Effect of H_2S on corrosion rate*	N	N	W	N	N	N	M	S	S	N	W	N	S	N
Multiphase flow calculation**	N	P	M	P	N	N	P	M	P	P	M	M	N	N
Max. temperature limit °C	140	150	150	150	140	150	100	140		115		150	120	120
Max. CO_2 partial pressure bar	10	10	20	20	10	20	20	20	70	17		10	20	
Open, **C**ommercial, **P**roprietary	O	O	P	O	O	O	P	C	C	P	P	P	C	P

* S - strong effect, M - moderate effect, W - weak effect, N - no effect

** P - point calculation, M - multiphase profile calculation, N - no multiphase flow calculation

B.6 Review of Tulsa CO_2 Corrosion Model

Dalayan et al, 1995 and 1998 proposed a mechanistic model for CO_2 corrosion rate prediction. According to this model, the overall CO_2 corrosion process has four main steps (Fig. B.12). The first step in CO_2 corrosion process is the formation of reactive species in the bulk. In this step CO_2 gas dissolves in water and then hydrate to form carbonic acid. Carbonic acid can directly reduce on metal surface or it can dissociate to bicarbonate ions first and then reduce on the metal surface as a cathodic reaction. The second step in CO_2 corrosion process is the transportation of cathodic reaction species (reactants) from the bulk to the surface of metal. The driving force for transporting these species to the metal surface is consumption of these species on the surface by cathodic reaction of corrosion, which causes a concentration gradient between bulk and metal surface. The third step in CO_2 corrosion process is electrochemical corrosion reaction on the metal surface. Electrochemical corrosion reaction can be divided into two main categories as anodic and cathodic reactions. The last step in CO_2 corrosion process is the transportation of corrosion products from the metal surface to the bulk solution. The driving force for this transportation is concentration difference between metal surface and bulk solution. For the scale forming condition, mass transfer happens through the scale layer. Mass transfer through the scale layer was considered as diffusion through porous media.

Dayalan et al. (1995) based on three main hypothesizes developed their model consists of a system fifteen equations and fifteen unknowns. The model is valid for steady state CO_2 corrosion. It incorporates chemical and electrochemical reactions, and mass transport (Eqs. B.12 through B.26). CO_2 corrosion rate can be predicted for non-scale forming conditions by solving the system fifteen nonlinear equations. The main hypotheses in this model are: i) the sum of the mass transfer rates of the reactants must be equal to the sum of the electrochemical reaction rates (for both cathodic and anodic reactions); and ii) the sum of the mass transfer rates of carbonic acid and bicarbonate is equal to the mass transfer rate of carbonate ions.

According to the first hypothesis, mass transfer rate of Fe^{2+} is equal to electrochemical reaction rate of the iron dissolution. Therefore:

$$K_{mt,Fe^{2+}}([Fe^{2+}]_s - [Fe^{2+}]_b) = 2 \times 10^{-3} F.K_{Fe^{2+}}[Fe^{2+}]_s exp\left\{\frac{(2-B)F(E_{corr}-E_{Fe^{2+}})}{RT}\right\} \ldots\ldots (B.12)$$

where K_{mt} is mass transfer coefficient which can be different for different ions. $[Fe^{2+}]_s$ is iron ion concentration on the metal surface, $[Fe^{2+}]_b$ is iron ion in the bulk solution, F is Faraday constant, K_{Fe} is electrochemical reaction rate constant of iron ions, B is transfer coefficient (the value of B is 0.5 for most of the reactions), R is the universal gas constant, T is absolute temperature, E_{corr} is corrosion potential, and E^o_{Fe} is standard potential of iron at temperature T.

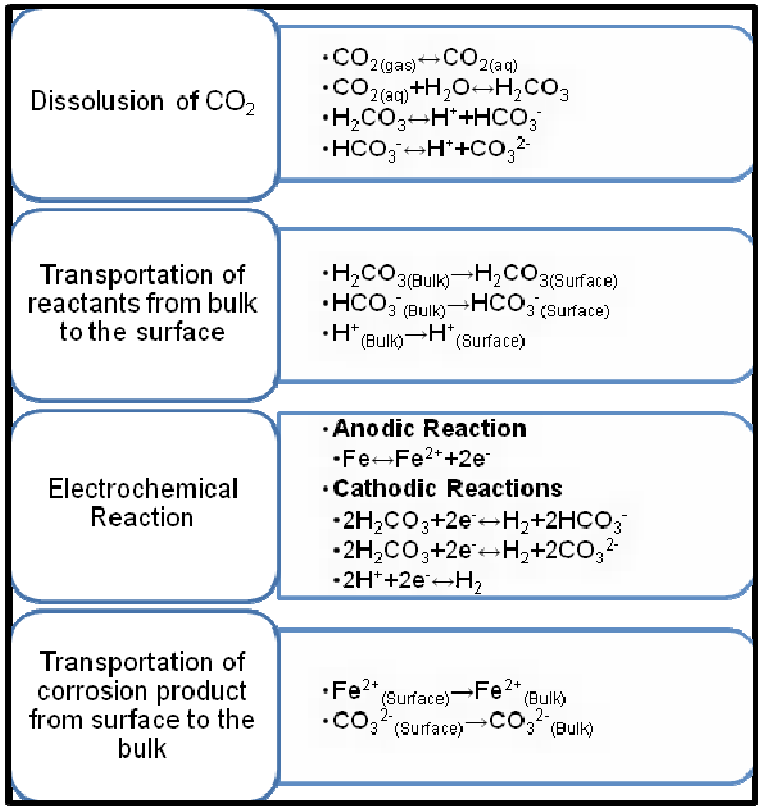

Fig.B.12 Summary of overall CO_2 corrosion process

From the second hypothesis, the sum of mass transfer rates of ($[H_2CO_3]$, $[HCO_3^-]$, $[H^+]$) are equal to the sum of electrochemical reaction rates of ($[H_2CO_3]$,$[HCO_3^-]$,$[H^+]$). Therefore:

$$K_{mt,H_2CO_3}([H_2CO_3]_b - [H_2CO_3]_s) + K_{mt,HCO_3^-}([HCO_3^-]_b - [HCO_3^-]_s) + K_{mt,H^+}([H^+]_b - [H^+]_s) = 2 \times 10^{-3} F.K_{H_2CO_3}[H_2CO_3]_s exp\left\{\frac{-BF(E_{corr}-E_{H_2CO_3})}{RT}\right\} + 2 \times 10^{-3} F.K_{HCO_3^-}[HCO_3^-]_s exp\left\{\frac{-BF(E_{corr}-E_{HCO_3^-})}{RT}\right\} + 2 \times 10^{-3} F.K_{H^+}[H^+]_s exp\left\{\frac{-BF(E_{corr}-E_{H^+})}{RT}\right\} \quad \text{....(B.13)}$$

Similarly, the sum of mass transfer rates of (H_2CO_3, HCO_3^-) is equal to the mass transfer rate of CO_3^{2-}. Therefore,

$$K_{mt,H_2CO_3}([H_2CO_3]_b - [H_2CO_3]_s) + K_{mt,HCO_3^-}([HCO_3^-]_b - [HCO_3^-]_s) = K_{mt,CO_3^{2-}}([CO_3^{2-}]_b - [CO_3^{2-}]_s) \quad \text{...(B.14)}$$

In addition, the sum of the cathodic reaction rates is equal to the sum of anodic reaction rates and it is equal to corrosion current density.

$$I_{H_2CO_3} + I_{HCO_3^-} + I_{H^+} = I_{Fe^{2+}} = 2 \times 10^{-3} F.K_{Fe^{2+}}[Fe^{2+}]_s exp\left\{\frac{(2-B)F(E_{corr}-E_{Fe^{2+}})}{RT}\right\} = 2 \times 10^{-3} F.K_{H_2CO_3}[H_2CO_3]_s exp\left\{\frac{-BF(E_{corr}-E_{H_2CO_3})}{RT}\right\} + 2 \times 10^{-3} F.K_{HCO_3^-}[HCO_3^-]_s exp\left\{\frac{-BF(E_{corr}-E_{HCO_3^-})}{RT}\right\} +$$

$$2 \times 10^{-3} F.K_{H^+}[H^+]_s exp\left\{\frac{-BF(E_{corr}-E_{H^+})}{RT}\right\} \quad \text{(B.15)}$$

Electrochemical cathodic and anodic reactions are expressed as:

$$I_{H_2CO_3} = 2 \times 10^{-3} F.K_{H_2CO_3}[H_2CO_3]_s exp\left\{\frac{-BF(E_{corr}-E_{H_2CO_3})}{RT}\right\} \quad \text{(B.16)}$$

$$I_{HCO_3^-} = 2 \times 10^{-3} F.K_{HCO_3^-}[HCO_3^-]_s exp\left\{\frac{-BF(E_{corr}-E_{HCO_3^-})}{RT}\right\} \quad \text{(B.17)}$$

$$I_{H^+} = 2 \times 10^{-3} F.K_{H^+}[H^+]_s exp\left\{\frac{-BF(E_{corr}-E_{H^+})}{RT}\right\} \quad \text{(B.18)}$$

$$I_{Fe^{2+}} = 2 \times 10^{-3} F.K_{Fe^{2+}}[Fe^{2+}]_s exp\left\{\frac{(2-B)F(E_{corr}-E_{Fe^{2+}})}{RT}\right\} \quad \text{(B.19)}$$

Carbonic acid dissociation reaction has two steps. Reaction rate constants for these two steps are:

$$K_1 = First\ Dissociation\ constant = \frac{[H^+]_s[HCO_3^-]_s}{[H_2CO_3]_s} \quad \text{(B.20)}$$

$$K_2 = Second\ Dissociation\ constant = \frac{[H^+]_s[CO_3^{2-}]_s}{[HCO_3^-]_s} \quad \text{(B.21)}$$

H^+ ions concentration also governed by water dissociation equilibrium described below.

$$K_w = water\ Dissociation\ constant = [H^+]_s[OH^-]_s \quad \text{(B.22)}$$

Equilibrium potential of all the cathodic and anodic species is a function of absolute temperature, and concentration of species based on the Nernst law.

$$E_{H_2CO_3} = E^o_{H_2CO_3} + \frac{RT}{2F} Ln\left\{\frac{[H_2CO_3]_s{}^2}{[HCO_3^-]_s{}^2 .[H_2]}\right\} \quad \text{(B.23)}$$

$$E_{HCO_3^-} = E^o_{HCO_3^-} + \frac{RT}{2F} Ln\left\{\frac{[HCO_3^-]_s{}^2}{[CO_3^{2-}]_s{}^2 .[H_2]}\right\} \quad \text{(B.24)}$$

$$E_{H^+} = E^o_{H^+} + \frac{RT}{2F} Ln\left\{\frac{[H^+]_s{}^2}{[H_2]}\right\} \quad \text{(B.25)}$$

$$E_{Fe^{2+}} = E^o_{Fe^{2+}} + \frac{RT}{2F} Ln\{[Fe^{2+}]_s\} \quad \text{(B.26)}$$

where $E^o_{H_2CO_3}$, $E^o_{HCO_3^-}$, $E^o_{H^+}$, and $E^o_{Fe^{2+}}$ are the standard potentials for reduction and oxidation reactions.

Fifteen unknowns are the six surface concentrations ($[H^+]_s$, $[HCO_3^-]_s$, $[Fe^{2+}]_s$, $[CO_3^{2-}]_s$, $[OH^-]_s$, $[H_2CO_3]_s$), four equilibrium potentials ($E^o_{H_2CO_3}$, $E^o_{HCO_3^-}$, $E^o_{H^+}$, and $E^o_{Fe^{2+}}$), the corrosion potential (E_{corr}), and current due to four reactions (I_{H2CO3}, I_{HCO3^-}, I_{H^+}, $I_{Fe^{2+}}$).

Figure B.13 shows the comparison between the CO_2 corrosion rate prediction using the model proposed by Dayalan et al. (1995) and experimental data.

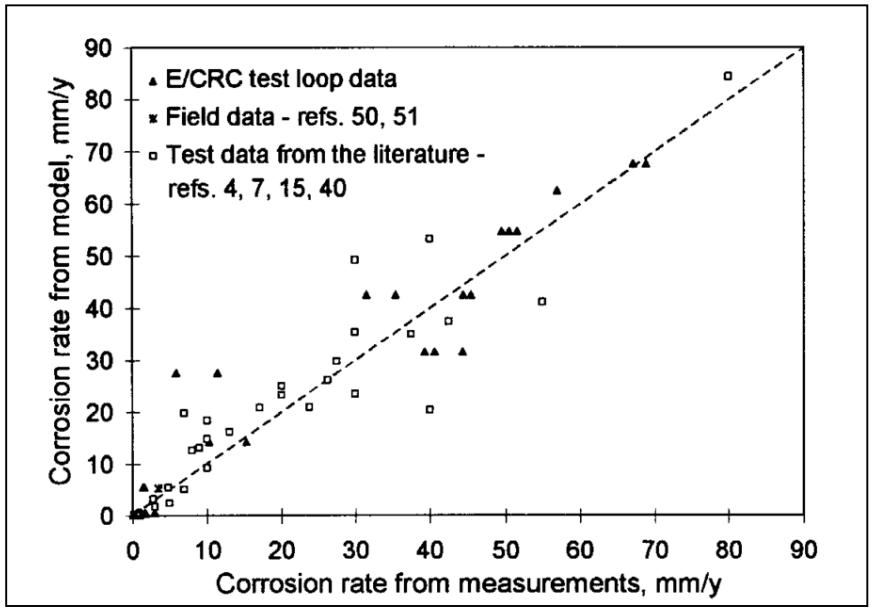

Fig.B.13 Predicted CO_2 corrosion rate vs. experimental data (Dayalan et al., 1995)

A.6 Modified Version of Tulsa CO_2 Corrosion Models for Non-Scale Forming Conditions

Based on the absolute reaction rate theory of Glasstone et al. (1939) for reactants to be converted into products, a transitory state is first reached, in which an "active complex" is formed. Formation of such a complex requires overcoming a free energy barrier of height ΔG#.

$$A + B \rightarrow [AB]^{\#} \rightarrow \text{Products} \quad \text{(B.27)}$$

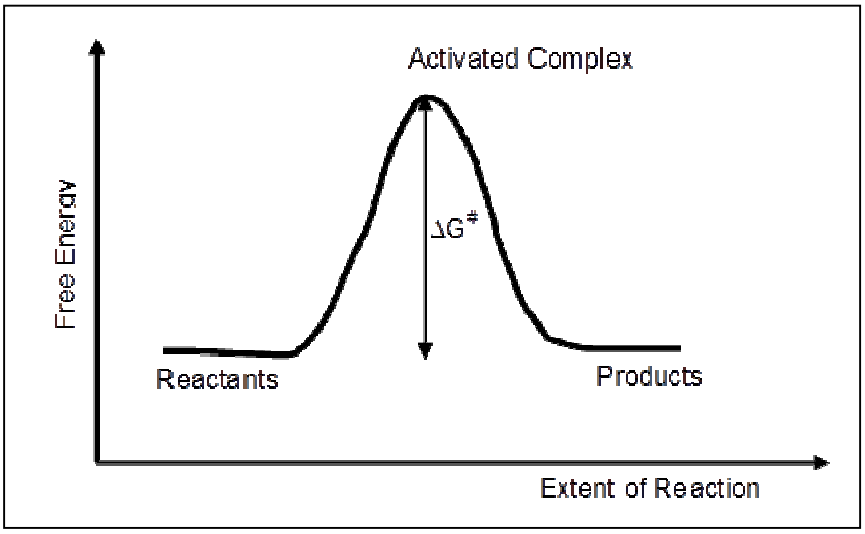

Fig.B.14 Change in free energy as a function of reaction extent

Thus, the rate of reaction (R_x) expressed as:

R_x = (Concentration of complex) × (Rate of passage over energy barrier)……(B.28)

When the activated complex is poised at the top of the energy barrier, its vibration rate (h ϑ) is just equal to the thermal energy (KT). Therefore,

h ϑ = KT ……(B.29)

where h is Plank's constant, ϑ is the frequency of vibration of complex, K is Boltzman's constant. Therefore, ϑ is the rate of passage of activated complexes over the energy barrier.

$$\vartheta = \frac{KT}{h} \quad \text{(B.30)}$$

Using (B.27) and (B.30):

$$R_x = [AB^{\#}]\frac{KT}{h} \quad \text{(B.31)}$$

Equilibrium constant for the formation of the activated complex is:

$$K^{\#} = \frac{[AB^{\#}]}{[A].[B]} \quad \text{(B.32)}$$

Also from thermodynamic

$\Delta G^{\#}$=-RTLnK$^{\#}$.....(B.33)

Therefore,

$$K^{\#} = exp\left\{-\frac{\Delta G^{\#}}{RT}\right\} \quad \text{(B.34)}$$

Using Eqs. (B.31), (B.32), and (B.34)

$$R_x = [A][B] \underbrace{\frac{KT}{h} exp\left\{-\frac{\Delta G^{\#}}{RT}\right\}}_{Reaction\ Rate\ Const.} \quad \text{(B.35)}$$

If we change the potential from E_o to E as shown in Fig. B.15, then the change in free energy will be determined as:

$\Delta G^{\#}=\Delta G_o^{\#}-\alpha nF(E-E_o)$ .....(B.36)

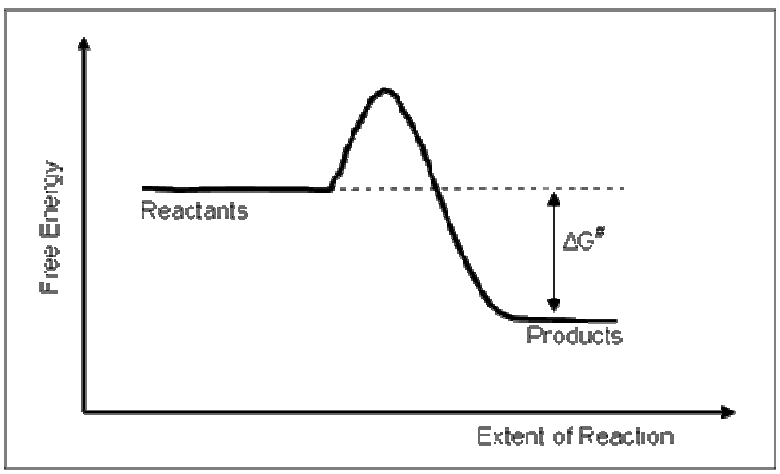

Fig. B.15 Change in free energy as a function of reaction extent

Using Eqs. (B.35) and (B.36)

$$R_x = \frac{KT}{h} exp\left\{-\frac{\Delta G_o^{\#} - \alpha nF(E-E_o)}{RT}\right\} \quad \text{(B.37)}$$

where parameter α is a measure of the symmetry of the free energy barrier. When α = 0.5, the degree of decrease in the free energy barrier in the forward reaction is the same as its degree of increase in the reverse direction. (α is between 0 and 1, but usually 0.5).

Total current "I" across a surface area of A is

$$I = (Rate\ constant).\underbrace{(C_{Surf})}_{[A][B]} nFA \ldots\ldots (B.38)$$

$$i = \frac{I}{A} = \frac{KT}{h} C_{Surf} nF exp\left\{-\frac{\Delta G_o^{\#} - \alpha nF(E-E_o)}{RT}\right\} \ldots\ldots (B.39)$$

or

$$i = \underbrace{\frac{KT}{h} exp\left\{-\frac{\Delta G_o^{\#}}{RT}\right\} C_{Surf} nF}_{i_o} exp\left\{\frac{\alpha nF(E-E_o)}{RT}\right\} \ldots\ldots (B.40)$$

i_o is called the exchange current density. The exchange current density represents the reaction rate in either direction at the equilibrium open circuit potential E_o. Equation (B.40) can be used in CO_2 corrosion model for modeling the current density of anodic and cathodic reaction.

Mass transfer rate of Fe^{2+} is equal to electrochemical reaction rate of the iron dissolution. Therefore:

$$K_{mt,Fe^{2+}}([Fe^{2+}]_s - [Fe^{2+}]_b) = nF\frac{KT}{h} exp\left\{-\frac{\Delta G^{\#}_{Fe^{2+}}}{RT}\right\}[Fe^{2+}]_s exp\left\{\frac{\alpha nF(E_{corr} - E_{Fe^{2+}})}{RT}\right\} \ldots (B.41)$$

Dayalan et al. (1995) assumed that the sum of mass transfer rates of ([H_2CO_3], [HCO_3^-], [H^+]) is equal to the sum of electrochemical reaction rates of ([H_2CO_3], [HCO_3^-], [H^+]) whereas cathodic reduction of carbonic acid produces bicarbonate and also cathodic reaction of bicarbonate produces carbonate ions which is not considered in this hypothesis. In this report the proposed hypothesis by Dayalan et al. (1995) was modified by assuming that mass transfer rate of each of the cathodic species is equal to the electrochemical reaction rate of that species under steady state conditions.

$$K_{mt,H_2CO_3}([H_2CO_3]_b - [H_2CO_3]_s) = \frac{KT}{h} exp\left\{-\frac{\Delta G^{\#}_{H_2CO_3}}{RT}\right\}[H_2CO_3]_s nF exp\left\{\frac{\alpha nF(E_{corr} - E_{H_2CO_3})}{RT}\right\} \ldots (B.42)$$

$$K_{mt,H^+}([H^+]_b - [H^+]_s) = \frac{KT}{h} exp\left\{-\frac{\Delta G^{\#}_{H^+}}{RT}\right\}[H^+]_s nF exp\left\{\frac{\alpha nF(E_{corr} - E_{H^+})}{RT}\right\} \ldots\ldots (B.43)$$

Therefore, one more equation will be added to the system of fifteen equations (B.12 to B.26) and there won't be any need for the hypothesis of Eq. (B.14) in which the sum of mass transfer rates of (H_2CO_3, HCO_3^-) is equal to the mass transfer rate of CO_3^{2-}. Rest of the model formulation will be similar to that of Dayalan et al. (1995). Research is in progress to solve the system of fifteen nonlinear equations and fifteen unknowns.

A.7 Review of Ohio H_2S Corrosion Rates Prediction Model

We are currently working on better understanding of H_2S corrosion by reviewing the H_2S corrosion models proposed by Ohio University.